Marine Geology 395 (2018) 301–319

Contents lists available at ScienceDirect

Marine Geology

journal homepage: www.elsevier.com/locate/margo

Malaysia Airlines flight MH370 search data reveal geomorphology and seafloor processes in the remote southeast Indian Ocean

Kim Picard[a,*], Brendan P. Brooke[a], Peter T. Harris[b], Paulus J.W. Siwabessy[a], Millard F. Coffin[c,d,e], Maggie Tran[a], Michele Spinoccia[a], Jonathan Weales[a], Miles Macmillan-Lawler[b], Jonah Sullivan[a]

[a] Geoscience Australia, Environmental Geoscience Division, GPO Box 378, Canberra, ACT 2601, Australia
[b] GRID-Arendal, Postboks 183, N-4802 Arendal, Norway
[c] Institute for Marine and Antarctic Studies, University of Tasmania, Private Bag 129, Hobart, Tasmania 7001, Australia
[d] School of Earth and Climate Sciences, University of Maine, Orono, ME 04473, USA
[e] Woods Hole Oceanographic Institution, Woods Hole, MA 02543, USA

ARTICLE INFO

Keywords:
Indian Ocean
Multibeam echosounder
Geomorphology
Processes
Deepsea
Seamount

ABSTRACT

A high-resolution multibeam echosounder (MBES) dataset covering over 279,000 km^2 was acquired in the southeastern Indian Ocean to assist the search for Malaysia Airlines Flight 370 (MH370) that disappeared on 8 March 2014. The data provided an essential geospatial framework for the search and is the first large-scale coverage of MBES data in this region. Here we report on geomorphic analyses of the new MBES data, including a comparison with the Global Seafloor Geomorphic Features Map (GSFM) that is based on coarser resolution satellite altimetry data, and the insights the new data provide into geological processes that have formed and are currently shaping this remote deepsea area. Our comparison between the new MBES bathymetric model and the latest global topographic/bathymetric model (SRTM15_plus) reveals that 62% of the satellite-derived data points for the study area are comparable with MBES measurements within the estimated vertical uncertainty of the SRTM15_plus model (± 100 m). However, > 38% of the SRTM15_plus depth estimates disagree with the MBES data by > 100 m, in places by up to 1900 m. The new MBES data show that abyssal plains and basins in the study area are significantly more rugged than their representation in the GSFM, with a 20% increase in the extent of hills and mountains. The new model also reveals four times more seamounts than presented in the GSFM, suggesting more of these features than previously estimated for the broader region. This is important considering the ecological significance of high-relief structures on the seabed, such as hosting high levels of biodiversity. Analyses of the new data also enabled sea knolls, fans, valleys, canyons, troughs, and holes to be identified, doubling the number of discrete features mapped.

Importantly, mapping the study area using MBES data improves our understanding of the geological evolution of the region and reveals a range of modern sedimentary processes. For example, a large series of ridges extending over approximately 20% of the mapped area, in places capped by sea knolls, highlight the preserved seafloor spreading fabric and provide valuable insights into Southeast Indian Ridge seafloor spreading processes, especially volcanism. Rifting is also recorded along the Broken Ridge – Diamantina Escarpment, with rift blocks and well-bedded sedimentary bedrock outcrops discernible down to 2400 m water depth. Modern ocean floor sedimentary processes are documented by sediment mass transport features, especially along the northern margin of Broken Ridge, and in pockmarks (the finest-scale features mapped), which are numerous south of Diamantina Trench and appear to record gas and/or fluid discharge from underlying marine sediments. The new MBES data highlight the complexity of the search area and serve to demonstrate how little we know about the vast areas of the ocean that have not been mapped with MBES. The availability of high-resolution and accurate maps of the ocean floor can clearly provide new insights into the Earth's geological evolution, modern ocean floor processes, and the location of sites that are likely to have relatively high biodiversity.

* Corresponding author.
E-mail address: kim.picard@ga.gov.au (K. Picard).

https://doi.org/10.1016/j.margeo.2017.10.014
Received 9 July 2017; Received in revised form 24 October 2017; Accepted 29 October 2017
Available online 08 November 2017

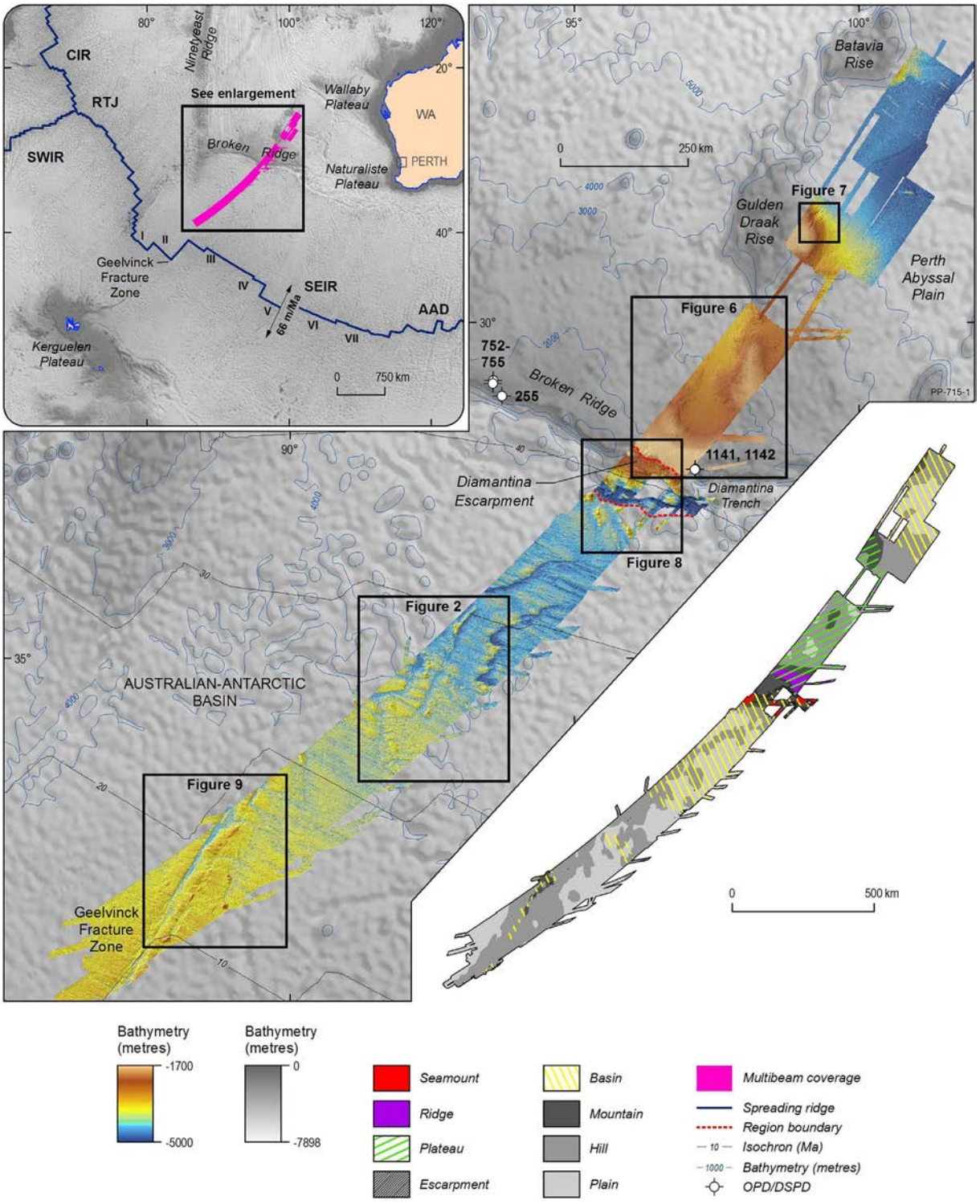

Fig. 1. Location map showing the multibeam bathymetry data combined with sun-illuminated relief collected in the search for MH370. The locations of Figs. 2 and 6 to 9 are displayed as well as the locations of DSDP and ODP drill sites 255 (Leg 26), 752–755 (Leg 121), and 1141/1142 (Leg 183). Upper left inset shows a map of the multibeam bathymetric coverage (pink) overlaid on the SRTM15_plus model (Olson et al., 2016). The map highlights the Southeast Indian Ridge (SEIR), estimated spreading rates of the SEIR (Argus et al., 2011), the magnetic isochrons (Müller et al., 2008), and interpreted SEIR segments (Small et al., 1999). SWIR: Southwest Indian Ridge; CIR: Central Indian Ridge; RTJ: Rodrigez Triple Junction; AAD: Australian-Antarctic Discordance; WA: Western Australia. Lower right inset is an excerpt of the Global Seafloor Geomorphic Feature Map (GSFM; Harris et al., 2014) corresponding to the search area. PP-715-1 is Geoscience Australia internal production number for this figure. (For interpretation of the references to colour in this figure legend, the reader is referred to the web version of this article.)

1. Introduction

Malaysia Airlines Flight 370 (MH370) was a scheduled international passenger flight that disappeared on 8 March 2014 while flying from Kuala Lumpur, Malaysia, to Beijing, China. In the ensuing multi-national effort to search for aircraft wreckage, a large area of ocean floor was mapped using ship-mounted multibeam echosounders (MBES), providing unprecedented detail in an otherwise remote area of the

ocean floor. The MBES data analysed in this paper were acquired because the only preexisting data were coarse-scale (e.g., ≤ 13 km horizontal resolution) satellite altimetry-based estimates of depth (Coffin et al., 2002; Hayes and Kane, 1994; Smith and Sandwell, 1997). The search for MH370 required improved resolution bathymetry to build an accurate geospatial framework for the second phase of the search—-high-resolution mapping of the seafloor using deep-towed, remotely operated (ROVs) and autonomous underwater vehicles (AUVs) to collect images, and high-resolution sidescan and multibeam data assisting in the search for aircraft wreckage (Picard et al., 2017a). The new shipboard multibeam dataset presented here thus represents the largest MBES coverage effort for the remote southeastern Indian Ocean region (Fig. 1; Picard et al., 2017a, b).

The Earth's vast marine realm remains little known compared to the terrestrial environment. In particular, accurately mapping the bathymetry of the ocean floor remains a major global challenge, with only 10%–15% of it mapped using MBES (Weatherall et al., 2015). In addition to mapping the bathymetry, MBES systems also record acoustic backscatter intensities, which are often useful for discriminating different types of seabed, such as hard rock and soft sediment (Siwabessy et al., 2017). These important MBES data outputs enable the fundamental physical characterisation of large areas of ocean floor that otherwise may lack any environmental observations. Importantly, MBES data and parameters derived from the data (e.g., rugosity, bedform geometry) can be used for inferring geological and oceanographic processes, and for identifying benthic habitats (Harris and Baker, 2012).

1.1. Aims and objectives

The scale at which seafloor geomorphic features can be mapped depends upon the resolution of the available bathymetric model. For example, mid-ocean ridges and ocean trenches are visible at a quite coarse resolution (10 s of km), whereas sand waves and gas-escape features can only be detected using finer resolution data (e.g., 10 s of m). The new MBES data provide a “window” of high-resolution data amidst an ocean region where only the most coarse, global bathymetry data were previously available. In this paper, we analyse the new bathymetric and backscatter intensity models to better describe the type and distribution of geomorphic features present in this window of the MH370 search area and compare these results with the seafloor geomorphic features identified in the Global Seafloor Geomorphic Features Map (GSFM; Harris et al., 2014). Importantly, this comparison helps to identify the minimum resolution of bathymetry data required to robustly map fundamental seafloor geomorphic features. We also use the high-resolution MBES data to provide insights into the geological evolution of the region and to interpret seabed geomorphic processes.

2. Study area

The MH370 search area is located in the southeastern Indian Ocean, ~1800 km west of southwest Australia (Fig. 1). The area mapped by MBES is 75– > 200 km wide and > 2500 km long, covering a total area of ~279,000 km^2 (21°S to 39°S; 87°E to 105°E; Fig. 1). Water depths range between 635 and 6300 m. In this study, we map the geomorphology of 240,000 km^2 of seafloor based on data collected between June 2014 and June 2016.

The known, large-scale seafloor features in this region include Batavia and Gulden Draak Rises, Perth Abyssal Plain, Broken Ridge, Diamantina Trench, and the Australian-Antarctic Basin (Fig. 1). The southern boundary of the study area lies ~150 km north of the Southeast Indian Ridge (SEIR), which marks the axis of active seafloor spreading forming the boundary between the Australian and Antarctic plates. Most data cover the area northeast of the Geelvinck Fracture Zone, which separates spreading ridge segments II and III (Fig. 1; Small et al., 1999), with most of the seafloor mapped formed in the period represented by segment III. Based on an isochron model for the region, the youngest seafloor mapped here is ~10 Ma, located ~270 km from the SEIR on segment III (Fig. 1; Müller et al., 2008).

2.1. Geological evolution

The geology and morphology of the southeastern Indian Ocean region have provided key information on the major tectonic and volcanic processes that drove the break-up of Gondwana (160 Ma) and the related formation and spreading of oceanic plates (Coffin et al., 2002; DeMets et al., 2010; Gaina et al., 2007; Gardner et al., 2015; Hayes and Kane, 1994; Müller et al., 1993; Small et al., 1999). The study area is centered on part of the Broken Ridge Large Igneous Province (LIP), which extends north from the Diamantina Escarpment (Fig. 1; Coffin and Eldholm, 1994; Coffin et al., 2002) and comprises extensive plains, ridges, rises, and seamounts. The south of the escarpment is a large trough (known as Diamantina Trench) and a series of spreading ridges, fracture zones (e.g., Geelvinck), deep fault valleys, and numerous presumably relict volcanoes (Fig. 1).

Prior to the onset of the rifting of Gondwana, Gulden Draak and Batavia Rises, along with the Naturaliste Plateau, were part of the macro-continent, incorporating what is now India, Australia, and Antarctica (Gardner et al., 2015). These components parted from the main continent at ~126 Ma, and by the Late Cretaceous, Broken Ridge and the Kerguelen Plateau formed one extensive submarine plateau of ~2 million km^2 (Coffin and Eldholm, 1994). Until ~40 Ma, sediments accumulated above the igneous basement, producing a sedimentary sequence dominated by chalks and limestones that is between 1 and 1.5 km thick (Rea et al., 1990). At ~40 Ma, rifting and seafloor spreading began at the newly formed SEIR and cut through the submarine plateau to form Broken Ridge and the Kerguelen Plateau LIPs (Fig. 1; Coffin and Eldholm, 1994; Coffin et al., 2000; Coffin et al., 2002; Karner and Driscoll, 1993). These provinces comprise iron and magnesium rich rocks that were erupted from the Kerguelen hotspot between ~130 and ~40 Ma (Coffin and Eldholm, 1994; Coffin et al., 2000; Duncan, 2002; Neal et al., 2002; Wallace et al., 2002). This occurred concurrently with the separation of the Indian Plate, and Batavia and Gulden Draak micro-continents, from the Australian and Antarctic plates and the subsequent migration of the Indian and Australian plates northwards (Coffin et al., 2000; Gardner et al., 2015).

The Broken Ridge and Kerguelen LIPs are now separated by the Australian-Antarctic Basin, which contains many abyssal hills that have formed at the SEIR since ~40 Ma, at an intermediate rate of spreading (~59–75 km/Ma; Coffin et al., 2002; Müller et al., 1993; Small et al., 1999). The southern margin of Broken Ridge records rifting and breakup with the Central Kerguelen Plateau. It is known as the Diamantina Escarpment and plunges > 5100 m from its crest (Broken Ridge, 638 m) into a deep trough (Diamantina Trench, 5800 m). The escarpment is delineated by a major southward-dipping normal fault, with a cumulative throw of > 5 km and overall dip of 20° (Pierce et al., 1989).

At the time of rifting, Broken Ridge was rapidly uplifted by ~2.5 km (in < 2–3 Myr) due to plate flexure (Karner and Driscoll, 1993; Rea et al., 1990). Drill cores show that the ridge was then subjected to subaerial erosion, with the eroded material accumulating on the north-facing slope of the ridge. These terrestrial deposits mark the start of sediment accumulation on the ridge during the Eocene (Rea et al., 1990). Subsequent subsidence of the ridge (~1100 m) led to the accumulation of pelagic ooze (> 120 m), in which is recorded as a transition from shallow to deeper-water organisms.

The SEIR near the southern margin of the study area is made of several relatively long (200–500 km) first-order segments of spreading centers that exhibit a gradual transition from a fast to a slow rate of spreading based on their morphology and segmentation (Fig. 1; Small et al., 1999). Limited MBES data in this area reveal a diffuse spreading axis that generally lacks a well-defined neovolcanic zone, and en-

echelon offsets characterised by higher-order segmentation of the ridges (Russo et al., 2009; Small et al., 1999).

2.2. Modern seafloor environment

Rates of seafloor sedimentation are usually low in the deep oceans, typically ~3 m/Myr (Hamblin and Christiansen, 2004). Benthic sediment can also be reworked downslope and winnowed by currents (tidal and oceanic), which usually dominate in shallower depths (< 2500 m). The southern part of the study area does not extend into latitudes of the Antarctic Circumpolar Current (ACC) that is expected to generate regular benthic storms (Harris et al., 2014). Nevertheless, a global bottom current model indicates a maximum value of 0.33 m/s occurs in the study area (Barnier et al., 2011), which is within the range of a "benthic storm" (Hollister, 1993).

Depths exceeding 4000 to 4500 m are below the Calcium Compensation Depth (CCD) and hence carbonate deposition in such areas is precluded (Berger and Winterer, 1974). Samples from the region suggest that sedimentation between Broken Ridge and the SEIR is minimal, with extensive areas of manganese nodule pavement (Kennett and Watkins, 1975; Kidd and Davies, 1978). Information on sedimentation in the southeastern Indian Ocean is sparse (Kidd and Davies, 1978; Whittaker et al., 2013), although seven drill sites have penetrated and recovered cores from Broken Ridge, in water depths of ~1000 to 1200 m (Fig. 1). These recovered > 100 m thick deposits of foraminiferal or foraminifer-bearing nanofossil ooze (Davies et al., 1974; Pierce et al., 1989; Coffin et al., 2000). Since the start of hemipelagic sediment deposition, sedimentation rates are estimated to be between 3 and 6 m/Myr (Rea et al., 1990; Coffin et al., 2000).

In their Global Seafloor Geomorphic Features Map, Harris et al. (2014) mapped abyssal hills (areas with relief between 300 m and 1000 m) and plains that represent 52% and 36% of the study area respectively (Fig. 1; Table 3). The most prominent discrete features that they mapped are basins and plateaus (40% and 17%, respectively; Table 3), as well as several seamounts.

3. Methods

3.1. MBES data

Data presented in this study were acquired by the MV *Fugro Equator*, MV *Fugro Supporter*, and the Chinese naval vessel *Zhu Kezhen* between June 2014 and June 2016. A total of 240,000 km^2 of high-resolution multibeam bathymetry data were acquired using a Kongsberg EM 302 (30 kHz, MV *Fugro Equator*) and EM 122 (12 kHz, MV *Fugro Supporter*), and a modified Reson Seabat 7150 (12 kHz, *Zhu Kezhen*). The resolution of the MBES instruments employed are provided in Table 1. Raw data from the Fugro vessels were post-processed, and processed data from the *Zhu Kezhen* were verified using the CARIS Hydrographic Information Processing System (HIPS) and CARIS/Sonar Image Processing Software (SIPS) v.7.1.2 SP2, following standard procedures (Buchanan et al., 2013). The processed data were exported as ASCII XYZ point cloud files. Bathymetry data were converted into 40 and 110 m grid formats via LASTools and Python, and imported into ArcGIS v.10.0 for spatial analysis.

Three-dimensional renders were produced by generalising the multibeam XYZ point clouds into a 40 m horizontal resolution raster grid using the average depth of all data within each grid cell. Grid cells with no data were filled with adjacent depth values using linear interpolation from surrounding data points in a radius of up to 5 cells. The 40 m grid was then converted into a RGB depth-colour tinted image, which was subsequently pan-sharpened with a 40 m resolution hill-shaded grid. The pan-sharpened image was then draped on the original depth grid in a 3D environment.

Multibeam backscatter data were collected by MV *Fugro Equator* and MV *Fugro Supporter*. Prior to commencing data acquisition for the search, Fugro calibrated its Kongsberg EM 302 multibeam echosounder aboard MV *Fugro Equator*, with the assistance of a Kongsberg engineer. This calibration ensures that backscatter intensities are consistent across different sectors over homogeneous seabed areas and for different ping modes (Lamarche and Lurton, 2017). Although this calibration provides consistency across sectors, the backscatter measurements remain relative as the system was not subjected to an absolute calibration. Post-processing using CARIS HIPS & SIPS software was done only for the data from MV *Fugro Equator*. This process involved running GEOCODER algorithms that performed radiometric and geometric correction, and mosaic blending between individual mosaics of survey lines (Fonseca and Calder, 2005). Batch processing was performed on backscatter data, and banding effects were highlighted and corrected for using dB offsets applied with the SIPS Template wizard. Mosaics were then created using Mosaic Editor. The final processed backscatter data were then gridded to 15 and 30 m horizontal resolution and exported as ESRI ASCII grids for analysis in ArcGIS v.10.0.

Sub-bottom profiles were acquired using a Simrad SBP300 (sweep frequency ranging from 2.5 to 6.5 kHz) along ~4900 line-kilometer to examine sediment accumulation. These data were collected simultaneously with the MBES data on MV *Equator* in the area between Batavia and Gulden Draak Rises only. The SBP300 profiles were analysed and processed using SonarWiz v.6. Time-varying gain was applied and depth measurements were calculated based on a sound speed of 1500 m/s.

3.2. Global seafloor model

The latest Shuttle Radar Topographic Model plus bathymetry (SRTM15_plus; Olson et al., 2016) for the study area has a pixel resolution of 15 min (~500 m). However, the model is controlled by relatively sparse sounding density, which in the worse case scenario is only controlled by altimetry data that has a horizontal resolution of 12.5 km (Becker et al., 2009). For the study area, this recent model used the same data as the SRTM30_plus (~1000 m pixel resolution), which was used to create the GSFM (Harris et al., 2014). Features mapped in the GSFM are assumed to have a spatial resolution of 3 × 3 grid points, with feature areas rounded to the nearest 10 km^2.

3.3. Geomorphological analysis

Feature names adhere to the International Hydrographic

Table 1
Technical specifications of the multibeam echosounders employed in the survey. The horizontal resolution at nadir is based on the beam width, while the vertical resolution is based on the signal wavelength and manufacturers specifications.

Vessel	MBES model	Manufacturer	Beam width (deg.)	Frequency (kHz)	Horizontal resolution at nadir between 600 and 6000 m (m)	Vertical resolution (m)
MV Fugro Equator	EM 302	Kongsberg	1 × 1	30	10–105	0.050
Zhu Kezhen	Seabat 7150[a]	Reson	1 × 1	12	10–105	0.125
MV Fugro Supporter	EM 122	Kongsberg	1 × 2	12	10–105 (across) 21–209 (along)	0.125

[a] Modified, upgraded version.

Table 2
Summary of the method used by Harris et al. (2014) to depict the features presented in the GSFM (METHOD 1) and modifications made to this method to depict Harris-scale (Method 2a) and fine-scale features (Method 2b) from the MBES dataset. All polygons were smoothed using ESRI PAEK algorithm with tolerances of 2 nm (METHOD 1) and 1 km (METHOD 2) unless specified. Final acceptance and digitisation of each feature types was undertaken at a spatial scale of 1:500,000.

Feature type	Definition based on IHO and Harris et al. (2014)	METHOD 1: GSFM method (Harris et al., 2014) (used SRTM30_Plus, ~1000 m)	METHOD 2: MBES modifications to METHOD 1 (used MBES model at 110 m)
Abyssal classification layers			
Plain	Extensive area of low-relief (< 300 m)	1. Calculated standard deviation using focal statistics based on a circle with a cell radius of 25 Classified the standard deviation values with < 75 and converted to polygons	**Method 2a** 1. Calculated standard deviation using focal statistics based on a circle with a cell radius of 250
Hill	Extensive area of medium-relief (300–1000 m)	1. Calculated standard deviation using focal statistics based on a circle with a cell radius of 250 Classified the standard deviation values with 75–250 and converted to polygons	1. Calculated standard deviation using focal statistics based on a circle with a cell radius of 250
Mountain	Extensive area of high-relief (> 1000 m)	1. Calculated standard deviation using focal statistics based on a circle with a cell radius of 250 Classified the standard deviation values with > 250 and converted to polygons	1. Calculated standard deviation using focal statistics based on a circle with a cell radius of 250
Discrete features			
Ridge	An elongated elevation of varying complexity, size and gradient. They also often separate basin features	1. Calculated Topographic Position Index (TPI) with circle radii of 50 and 100 2. Classified TPI values into 3 classes: > −200, −200 to –1000, < −1000 and converted to polygons Deleted polygons with −200 to −1000 m that were not adjacent to polygons of < −1000 Deleted polygons > 1000 m relief and < 100 km^2	**Method 2a** 1. Calculated TPI values from circle radii of 50 and 100 because the same radii used by Harris et al. failed due to the narrow width of the dataset (70 to 160 km) 2. Classified using same classes but no polygons were returned from the TPI with radius of 50 **Method 2b** Ridges with TPI radius up to 15 times smaller were used (Method 1: 50 ∗ 1000 m versus Method 2: 30 ∗ 110 m). 1. Calculated TPI values from circle radii of 30, 50, and 100 2. Classified TPI values from 100 radius into two classes: < 100 and > 100 and TPI values from 30 and 50 radii into two classes: < 20 and > 20 3. Converted to polygons 4. Deleted polygon with TPI < 100 and < 20 and area < 50 km^2 and < 1 km^2 respectively 5. Selected polygons from finer-scales that were located within broader-scale polygons Selected ridges from spreading fabric south of Diamantina Escarpment based on the TPI calculated from radius 30
Canyon	An elongated, narrow, steep-sided depression that generally deepens down-slope.	1. Calculated TPI with circle radii of 3, 5 and 10 2. Classified TPI values into 2 classes: > 50 and < 50 and converted to polygons Selected only polygons with TPI value > 50 and that extended over depth range of 1000 m and incised > 100 m into slope	**Method 2b** Canyons were derived from similar scales but edges were better defined here 1. Calculated TPI using radius of 30 with values < −25 2. Selected only polygons that extended over depth range of 1000 m and incised > 100 m into slope.
Escarpment	An elongated, characteristically linear, steep slope separating horizontal or gently sloping areas of the seafloor.	1. Calculated slope with radius of 1 2. Classified slope values into 2 classes > 5° and < 5° and converted to polygons 3. Merged polygons with < 5° slope and area of < 5km^2 that intersected polygons with > 5° slope Deleted polygons with area < 100 km^2	**Method 2a** Escarpments were depicted using similar scales, but smaller area polygons were kept 1. Deleted polygons with area < 0.1 km^2
Basin	A depression more or less equidimensional in plan and of variable extent.	1. Selected most shoal, closed, 100 m, bathymetric contours Classified major ocean basins (> 800 km^2), and small basins (< 800 km^2)	**Method 2a** Only small basins (< 800 km^2) were identified. Because of the limited width of the dataset, large basins could not be defined
Plateau	A large, relatively flat elevation that is higher than the surrounding relief with one or more relatively steep sides.	Picked manually using 100 m contours	**Method 2a** Additionally used polygons derived from slope < 1.5°
Seamount	A distinct generally equidimensional elevation greater than 1000m above the surrounding relief as measured from the deepest isobath that surrounds most of the feature.	Stage 1 – Identification of feature peaks: 1. *1st method*: Calculated maximum height using focal statistics with annulus radii incrementing by 5 and between 5 to 50 2. Subtracted each 10 layers from topographic model and classified to identify areas > 1000 m. 3. Calculated the centroid of these areas 4. *2nd method*: Inverted SRTM30 model and filled sink holes from hydrology tool 5. Subtracted the results to SRTM30 grid and where difference was > 1000 m, calculated the	**Method 2a** Stage 1 – Identification of feature peaks: 1. Used 50 and 150 radii as larger radii did not pick additional features due to the size of the features in the dataset (< 15 km in diameter) 2. Calculated 2 additional focal statistics using outer radii of 30 and 40 with inner circle radius of 500 m 3. Selected peaks from radius 50 that matched the centroids from the radius 30 Stage 2 – Seamount base identification 1. Created polygons from TPI with outer circle radii of 50 and 100 with values > 50

(*continued on next page*)

Table 2 (*continued*)

Feature type	Definition based on IHO and Harris et al. (2014)	METHOD 1: GSFM method (Harris et al., 2014) (used SRTM30_Plus, ~1000 m)	METHOD 2: MBES modifications to METHOD 1 (used MBES model at 110 m)
		centroid Stage 2 – Seamount base identification 1. Calculated TPI with outer circle radii of 5, 10 and 15 2. Classified TPI values with > 50–60 and created polygons Selected polygons corresponding to centroids determined in stage 1	2. Selected polygons that were within 10 km of the peaks detected in Stage 1 and with area > 10 km^2 Final polygons were smoothed using PEAK algorithm with 2 km tolerance
Knoll (New)	A distinct elevation with a rounded profile less than 1000 m above the surrounding relief as measured from the deepest isobath that surrounds most of the feature.	NA	**Method 2b** Stage 1 – Identification of feature peaks: 1. Peaks > 500 m: Used same method as seamounts 2. Peaks > 250 m: For Stage 1, used outer radius of 30 and areas > 1 km^2 3. Divided polygons that encompassed more than one feature and calculated centroids Stage 2 – Seamount base identification 1. Calculated TPI with outer circle radius of 50 2. Selected polygons were manually reshaped to match feature base Final polygons were smoothed using PEAK algorithm with 2 km tolerance
Trough	A long depression generally wide and flat bottomed with symmetrical and parallel sides. They are also commonly open at one side.	Digitised manually based on the interpretation of 100 m bathymetric contours	**Method 2b** 1. Calculated TPI with outer circle radii of 50 and 100 2. Classified TPI values into two classes with values < 50 and > 50 and converted to polygons Selected polygons located between two escarpments > 100 km^2, with areas > 10 km^2 and located within Diamantina Escarpment region
Valley (new)	An elongated depression that generally widens and deepens down-slope.	Identified only shelf valleys defined by incision > 10 m and length > 10 km	**Method 2b** Used same method as for troughs, but selected only polygons located in the region South of Diamantina Escarpment
Fan	A relatively smooth, depositional feature continuously deepening away from a sediment source commonly located at the lower termination of a canyon or canyon system.	Picked manually based on 100 bathymetric contours forming a concentric series that show expanding spacing seaward away from the base of slope.	**Method 2b** Picked manually. In most cases, these features were very subtle; their toe is the most prominent part of the feature and their upper reach is not well defined. Therefore, only the most obvious features were identified, while their upper boundaries were more or less inferred
Hole (new)	A depression of limited extent with all sides rising steeply from a relatively flat bottom.	NA	**Method 2b** Picked manually from visual inspection of bathymetry and shaded-relief (azimuth 315°; elevation 45°; exaggeration 3 ×) layers

Organisation's nomenclature for geomorphic features (IHO, 2013) and modifications made by Harris et al. (2014), including shape, length, and height (Table 2). Geomorphological features were depicted in ArcGIS v.10.1 using a series of raster layers derived from the bathymetry data at 110 m resolution. This resolution was used because it encompasses the entire range of depths encountered in the area (maximum depth of 5800 m) and associated MBES beam footprint. This resolution was 83 times greater than the SRTM30_plus bathymetry model.

Where possible, we mapped two scales of features from the new data (Table 2): 1) broad-scale features, which followed the method of Harris et al. (2014), to enable direct comparison with the GSFM (Method 2a); and 2) fine-scale features, which followed as closely as possible the method of Harris et al., but where the minimum feature dimensions were reduced to fully utilise the high-resolution data (Method 2b). For example, in the GSFM, features were mapped using various spatial analysis algorithms and manual digitisation at a spatial scale of 1:500,000 (Method 1; Table 2), whereas we identified ridges using focal analyses that are based on radii up to 7% of the size of those used in the GSFM. As a novel addition to the analysis of data at such a fine-scale, backscatter data were also analysed for each feature type and box plots produced for each mapped feature type.

The geomorphology database for the study area was projected using the coordinate system UTM zone 46 South and the WGS84 datum. To gauge the range and scale of features that can be identified using the new MBES data compared to the SRTM15_plus, which is typically the only bathymetric data available for the deep ocean, a comparison was made with the seabed features identified for the study area in the GSFM (Harris et al., 2014). We also specifically compared these bathymetric models to capture the increase in depth accuracy.

4. Results

4.1. General comparison with GSFM

The new MBES data for the study area greatly improve our knowledge of its bathymetry and geomorphic features (Fig. 2). Comparing the MBES depth measurements with the corresponding latest global topographic/bathymetric model (SRTM15_plus) depth estimates suggests that nearly 62% of the global-model data in the study area fall within its estimated vertical uncertainty (± 100 m, Smith and Sandwell, 1997; Fig. 3a). However, this comparison also shows that > 38% of the global data show discrepancies with the co-located MBES data of > 100 m, in places by as much as 1900 m. Although these large depth discrepancies (> 500 m) are distributed throughout the mapped area, they are particularly prominent in the Broken Ridge – Diamantina Escarpment area and cover only about 1% of the total area (Fig. 3b). For example, the MBES soundings in Diamantina Trench are much deeper than the global-model's depth estimates (> 500 m), and

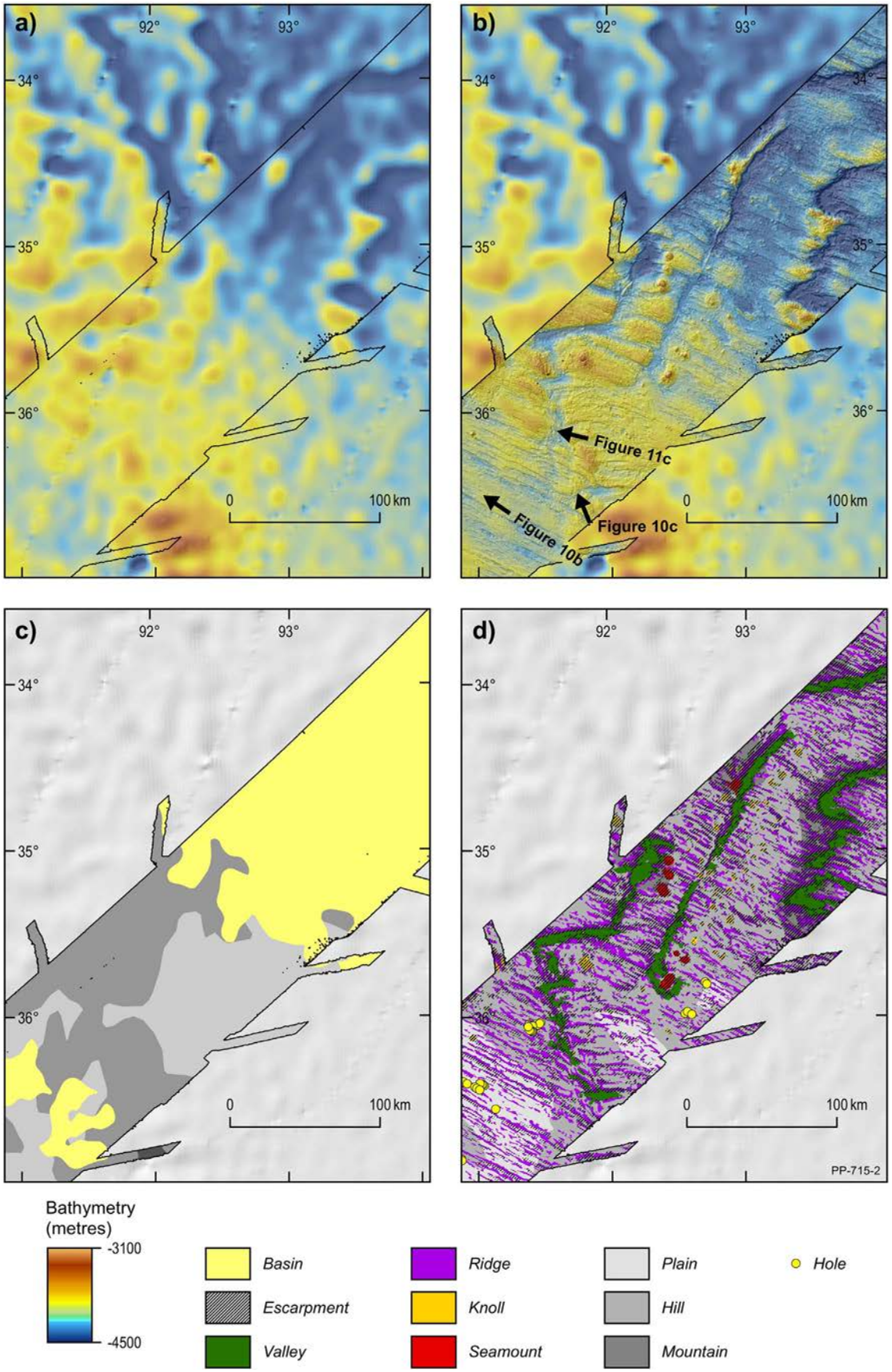

Fig. 2. Comparison between the SRTM15_plus model (a) and the MBES model (b), and associated geomorphic maps overlaid on sun-illuminated relief of the SRTM15_plus model (c and d, respectively) for an area south of the Diamantina Trench. Fig. 2b also indicates the viewing direction of the 3D images presented in Figs. 10 and 11. Location shown in Fig. 1. PP-715-2 is Geoscience Australia internal production number for this figure.

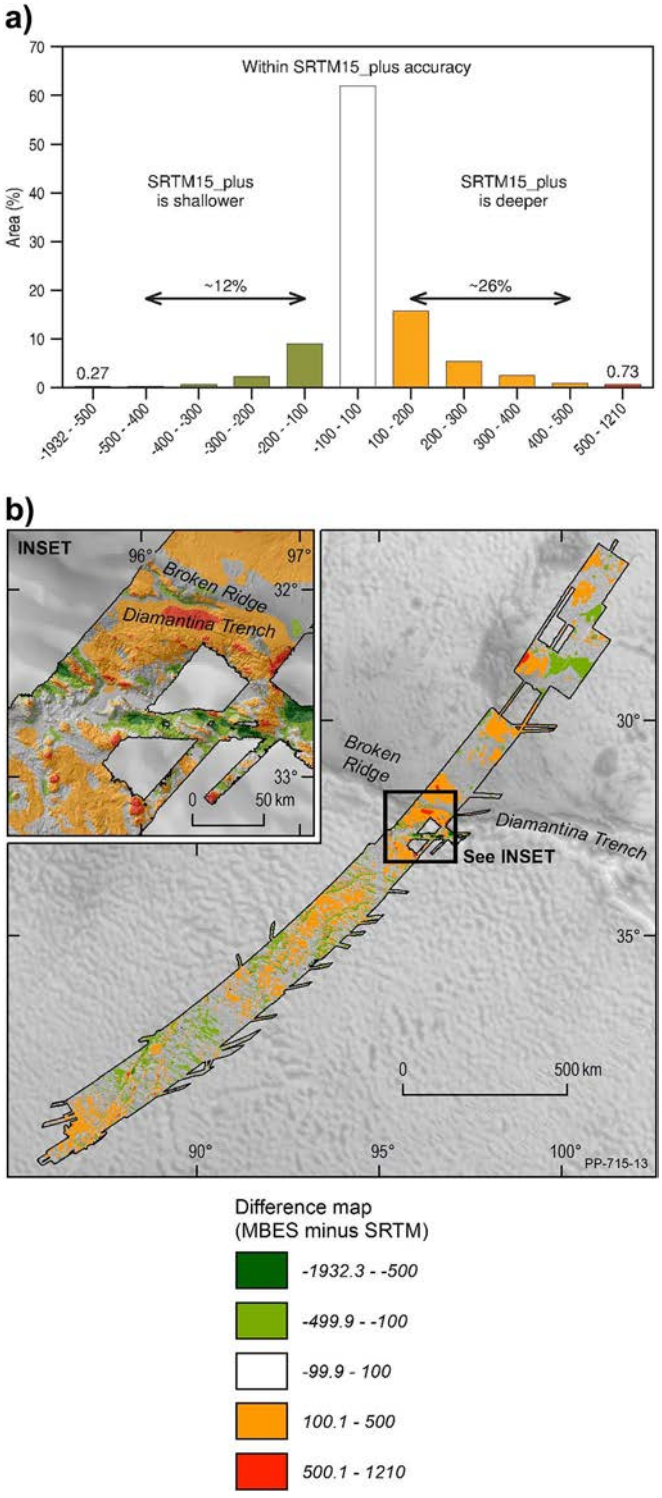

Fig. 3. Distribution histogram (a) and difference map (b) between the MBES and SRTM15_plus models. Vertical resolution of the SRTM15_plus model is estimated at best to ± 100 m (Becker et al., 2009; Smith and Sandwell, 1997). PP-715-13 is Geoscience Australia internal production number for this figure.

areas adjacent to the ridge crest are much shallower.

Based on the GSFM (Harris et al., 2014), the entire seabed of the study area lies within the abyssal depth class. In the GSFM, hills are the dominant geomorphic feature (52%), followed by plains (36%) and mountains (11%) (Table 3). In contrast, geomorphic mapping using the MBES data indicates hills cover 65% of the study area, while higher relief/mountainous areas cover 16%, and are mainly confined to the Diamantina Escarpment; plains cover ~19% and are evenly distributed across the study area (Table 3). Compared to the GSFM, the percentage of total rugged terrain (i.e., hills and mountains) mapped using the MBES data increased from 63% to 81% (Tables 2 and 3). There are also differences in coverage and number of instances of the five common feature types mapped at the same scale using the MBES and GSFM datasets (Table 3). For example, the dominant features in terms of coverage changed from basins and plateaus (57% of the total area in GSFM but 3% using the MBES data) to escarpments, which increased from 2% (GSFM) to 11% (MBES).

In addition to the discrete features present in the GSFM, the high resolution MBES data enabled the identification of an additional six types of features covering nearly 7% of the seafloor. These include fans, peaks, valleys, canyons, troughs, and holes (Table 3). If we also include escarpments covering areas of < 100 km^2 (not included at this scale in the GSFM) the total coverage of escarpments increases from 2% in the GSFM to 17% in the MBES classification (Table 3). Backscatter data analysis of these fine-scale feature types also shows that fans and plateaus return the lowest backscatter averages (− 40.1 and − 40.6 dB, respectively), and basins and troughs the highest (each − 28.4 dB; Fig. 4). Even though there is a general trend in the average backscatter between the geomorphic features, the discrepancies and absolute values observed are only a relative measure as the MBES backscatter data were not absolutely calibrated (see Section 3.1).

4.2. Seabed features and processes – utility of MBES data

Based on the new MBES data, we identified three distinctive geographical regions (Fig. 1) in the study area with unique assemblages of geomorphic features at a range of scales: 1) north of Broken Ridge (33.7% of the study area); 2) Diamantina Escarpment (4.7%); and 3) south of the Diamantina Trench (62.8%; Table 4). Region boundaries are defined by the isobath along the crest of Broken Ridge (boundary between regions 1 and 2), and the ~4200 m isobath immediately south of Diamantina Trench (boundary between regions 2 and 3; Fig. 1).

4.2.1. North of Broken Ridge

Here, water depths range between 634 and 5800 m, the seafloor has gradients < 5° (~95% based on the total area covered by escarpments, Table 4), and backscatter intensities are overall low (< − 32 dB, Fig. 6b). Large-scale features include the western margin of the Perth Abyssal Plain, the flanks of Batavia and Gulden Draak Rises, and the basin and rise that adjoin Broken Ridge (Fig. 1). Fine-scale features identified include plateaus and ridges, a large depression, and escarpments (Fig. 6).

To the north, the Perth Abyssal Plain is relatively featureless (Fig. 5), while the eastern flanks of Gulden Draak and Batavia Rises are dissected by channels and canyons (Fig. 7). Three of the total nine canyons (≤ 43 km long and two of them with > 1000 m depth range) occur in this region and represent about 68% of the total area covered by canyons (Fig. 5 and Table 4). Sub-bottom profiles collected across these areas show that a laterally persistent surficial sedimentary unit > 300 m thick (> 400 ms TWT) overlies basement (Fig. 7b). This deposit is stratified and divided by strong and conformable reflectors into three acoustic sub-units (A–C). In contrast, where mass transport is evident on the seafloor, surficial sediments exhibit chaotic internal bedding (Fig. 7b).

Broken Ridge (the elevated feature north of the Diamantina Escarpment) generally has subtle relief and includes one of the few large plateaus present in this region (Fig. 6). Approximately 70 km northeast of the escarpment is a large semi-circular depression (~10,000 km^2, 90 km diameter, 500 m relief; Fig. 6a). The MBES data reveal that the northern flank of Broken Ridge and the flanks of the large depression are dissected by numerous cross-cutting retrogressive slumps and debris flows (Fig. 6a). Debris fans, which are only mapped in this region (Fig. 5) extend out into the depression for > 150 km and

Table 3
A comparison of geomorphic features mapped using the SRTM15_plus model and the MBES data.

	Method 1 (GSFM)			Method 2a (MBES)		
	Area (km^2)	Area (%)	# of instances	Area (km^2)	Area (%)	# of instances
Abyssal layer classes						
Hills	124,317	52	26	154,287	65	11
Plains	86,850	36	17	45,406	19	27
Mountains	27,238	11	8	38,712	16	13
Total	238,405	100	51	238,405	100	51
Discrete features						
Basin	95,652	40	6	34	0.014	3
Plateau	41,655	17	1	7,658	3	12
Escarpment	5,000	2	9	26,776	11	29
Ridge	4,128	2	1	670	0.3	5
Seamount	1,509	1	4	1,279	0.6	19
Total	147,944	62	22	36,629	14.9	68
Additional discrete features (Method 2b)						
Escarpment (< 100 km^2)				14,077	5.9	2,311
Valley				9,849	4.1	26
Trough				2,734	1.1	12
Fan				2,220	0.9	8
Knoll				1,115	0.5	138
Canyon				203	0.1	9
Hole				NA	NA	44
Total				16,121	6.7	237

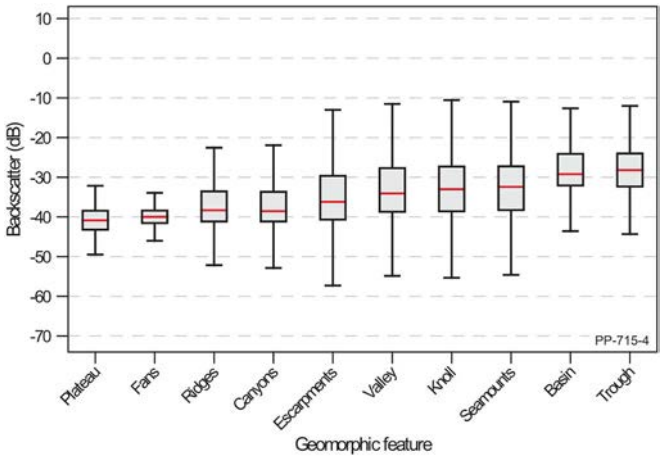

Fig. 4. Box plot showing backscatter intensity variations for geomorphic feature types mapped in this study. PP-715-4 is Geoscience Australia internal production number for this figure.

sediment lobes sit ≤10 m above the surrounding seafloor (Fig. 6a). Areas that have been affected by mass transport cover ≥10% of the seafloor in this region.

Two small, apparently relict volcanoes (sea knolls; ~250 m in height) sit atop the plateau northeast of the large depression (Fig. 6). Both volcanoes are characterised by high backscatter intensities compared to the surrounding seafloor, suggesting little sediment cover (Fig. 6b).

4.2.2. Diamantina Escarpment

This area has > 5000 m of vertical relief, from the crest of Broken Ridge (634 m) to the base of Diamantina Trench (> 5800 m; Fig. 8). Slopes commonly exceed 10° and along the margins of the trench reach > 35°. Large-scale seabed features include escarpments (≤1200 m high), plateaus, ridges, and the Diamantina Trench. In terms of geomorphic vocabulary, the trench is classified as a "trough" because it contains a flat floor ≤10 km wide (Table 2), indicating sediment infilling. Generally, the seabed in the Diamantina Trench is dominated by high backscatter intensities (Fig. 8b).

Six submarine canyons (10 km long and four of them exceeding a 1000 m depth range) are incised in the Diamantina Escarpment, extending downslope from around 2800 m depth (Fig. 8c). Most of these features are characterised by low to intermediate backscatter intensities (> −22 dB; Fig. 4). High backscatter intensity and lineaments indicate that bedrock is exposed in places at and near the top of Broken Ridge and at the Diamantina Escarpment to a depth of 1350 m (Fig. 8). Two large ridges are exposed on a plateau (~40 km in width; 1295 km^2) within the Diamantina Escarpment (Fig. 8). These ridges are ~12 by ~25 km and rise ≤700 m above the surrounding seafloor, with slopes of ≤50° on their southern flanks. A third similar ridge sits within the Diamantina Trench (30 km wide; 237 km^2; Fig. 8) and rises > 1200 m above the bottom of the trench (slopes > 20°;Fig. 8).

4.2.3. South of Diamantina trench

The seafloor south of the Diamantina Trench (depth range 2200 to 5000 m) is complex, with a series of ridges, often cut by deep valleys, and seamounts and sea knolls (Fig. 9). This area is also characterised by backscatter intensities that decrease towards the south (Fig. 9b). Ridges dominate in this region, both in terms of overall presence (79% of all ridges, Fig. 5) and proportional area to this region (~27%; Table 4). Ridges here are abyssal hills, a dominant component of seafloor spreading fabric. Individual ridges extend horizontally with continuous crests for > 70 km (Fig. 9). The south facing flanks of these ridges commonly form escarpments (> 100 km^2 in area), with slopes of ≤35°, and these features are most common in this region (> 84%, Table 4; Figs. 5, 9c). Large valleys cross-cut ridges and escarpments (Figs. 2d and 9c) and are present only in this region, occupying > 4% of the whole area (Fig. 5). These valleys appear to have formed by faulting that is related to fracture zones, and the adjacent ridges record horizontal offset and deformation. On the eastern side of the fracture zones, ridges are deformed towards the south, while on the western side they are deformed towards the north, indicating right-lateral motion of the original transform fault (Fig. 9a). The largest valley forms part of the Geelvinck Fracture zone. It has an area of > 2350 km^2, is ≤900 m deep and 8 km wide, with steep valley walls (> 30° slope; Fig. 9a).

There are 17 seamounts (> 1000 m relief) and 137 sea knolls (> 250 and < 1000 m relief) south of Diamantina Trench (only 1 sea knoll occurs outside this region; Fig. 5; Table 4). Seamounts cover < 1% of the study area (Table 4), occur as isolated features and in chains

Table 4
Geomorphic analysis statistics. The results are divided in overall area and by region. The overall section includes the mean backscatter value for each discrete feature. Blue cells highlight the new features identified compared to the GSFM features. Pink cells highlight the dominating region for each feature in terms of total area. Green cells highlight the dominating region for each feature in terms of normalised area, i.e. the feature percent area is calculated proportionally to the size of the region.

	Overall (238,404 km²)			North of Broken Ridge (86,889 km²)			Diamantina Escarpment (11,120 km²)			South of Diamantina Trench (140,396 km²)		
Feature	# of Instance	Area (%)	Backscatter mean (dB)	# of Instance	Area per feature total area (%)	Area proportional to region size (%)	# of Instance	Area per feature total area (%)	Area proportional to region size (%)	# of Instance	Area per feature total area (%)	Area proportional to region size (%)
Abyssal class		**100**			**32.7**			**4.7**			**62.8**	
Hill	7	64.7	NA	9	32.9	58.5	1	0.0	0.6	9	67.0	73.6
Plain	27	19.0	NA	13	50.4	26.3	0	0.0	0.0	2	49.6	16.0
Mountain	13	16.2	NA	5	34.1	15.2	1	28.5	99.4	14	37.4	10.3
Discrete feature												
Ridge	3166	20.6	-35.3	332	12.4	7.0	71	8.9	39.0	2785	79	27
Escarpment	2340	17.1	-34.1	203	3.9	1.9	38	12.5	45.8	2099	83.6	26.3
Valley	26	4.1	-32.9	0.0	0.0	0.0	0.0	0.0	0.0	26	100.0	7.0
Plateau	9	3.2	-40.6	5	79.8	7.0	5	20.2	13.9	0.0	0.0	0.0
Trough	12	1.1	-28.4	0.0	0.0	0.0	12	100.0	24.7	0.0	0.0	0.0
Fan	8	0.9	-40.1	8	100.0	2.7	0.0	0.0	0.0	0.0	0.0	0.0
Knoll	138	0.5	-33.1	1	0.1	0.0	0.0	0.0	0.0	137	99.9	0.8
Seamount	17	0.5	-32.3	0.0	0.0	0.0	0.0	0.0	0.0	17	100.0	0.8
Canyon	9	0.1	-37.7	3	68.5	0.2	6	31.5	0.6	0.0	0.0	0.0
Basin	3	0.0	-28.4	0.0	0.0	0.0	3	100.0	0.3	0.0	0.0	0.0
Hole	44	NA	NA	0.0	0.0	0.0	0	0.0	0.0	44	100.0	0.0

(Figs. 8 and 9), and also commonly form semi-concentric structures with rugged flanks (≤ 1500 m high, diameters 500 to > 15 km, slopes 10°–30°). The largest seamount occurs near Diamantina Trench (315 km^2; Fig. 8), but most lie adjacent to valleys, with diameters of ~4 km and variable backscatter intensities (Figs. 2 and 9). The smallest seabed features observed in the MBES data are small circular depressions (200–800 m diameter, 1–10 m deep) that likely represent pockmarks (Fig. 9c).

5. Discussion

5.1. Mapping at different resolutions

A comparison of the new MBES data with the SRTM15_plus model reveals that the method used to create the satellite-derived bathymetry is robust considering the small amount (< 1%; Smith et al., 2017) of sounding data that were available for calibration (Smith and Sandwell, 1997). The approximate mean vertical depth discrepancy between the STRM15_plus depth estimates and the corresponding MBES data is around 100 m (Fig. 3a), which represents about 2.5% of the average depth of the study area (3800 m). This discrepancy is also observed when comparing a more extensive area, e.g. including the transit data from the flight MH370 search (Picard et al., 2017b). The discrepancy correlates with the uncertainties associated with conversion between the two speeds of sound (fathoms/s versus m/s) in seawater used to calculate depth data between institutions (Smith, 1993). Therefore, the mean depth (averaged over roughly 100 km by 100 km patches; Smith, 1993) of the STRM15_plus model is consistent with its estimated level of accuracy. However, the greatest discrepancies are found in areas of high-relief in the seabed and/or thick sediment cover (Smith and Sandwell, 1997), such as observed here within Diamantina Escarpment (Fig. 5; see also Picard et al., 2017b). Although the SRTM15_plus model appears robust in the remote study area, its resolution limits its application in seabed mapping to large-scale features, such as those mapped in the GSFM using the SRTM30_plus model (Harris et al., 2014).

In contrast, the high-resolution MBES data enable the detection of much finer-scale seafloor features than the GSFM (Fig. 2). In particular, the extensive area previously mapped as abyssal plain and basin, which are considered as being mostly flat and featureless, are much more complex than previously depicted (Fig. 2). Overall, the percentage of rugged terrain (i.e., hills and mountains) able to be mapped using MBES increased by almost 20% compared to the GSFM (Table 3; Supplement material). Also, the five common types of large-scale features identified—ridges, seamounts, plateaus, basins, and escarpments—cover smaller areas than previously mapped, but the number of such features is greater (Table 3; Supplement material). This reduction in terms of coverage (especially plateau and basin) occurs because the large-scale features in the GSFM were captured using the global SRTM30_plus model from which features were mapped at a scale exceeding the width of our study area (~100 km). Also, most features mapped with the MBES data are smaller and have more irregular boundaries than the same features defined in the GSFM. This is due to the coarse resolution of the SRTM30_plus data used in the GSFM analysis, in which features are amalgamated if they cannot be entirely resolved in the coarser data. For example, even large features, such as the trough corresponding to Diamantina Trench (30 km wide - clearly identified in the MBES data; Fig. 8) were not resolved in the GSFM. Instead, the coarse resolution data only resolved the shallow escarpments and large ridges respectively bounding and located within the trough.

Geomorphic analysis of the MBES data also doubled the number of discrete feature types identified (Table 3; Supplement material). These features provide insights into the geological evolution of the region, in terms of both structural/tectonic and modern sedimentary processes (Figs. 10 and 11). For example, the thousands of NW-SE trending ridges south of the Diamantina Escarpment preserve seafloor spreading fabric that was created along the SEIR (Fig. 10b). In contrast, the escarpments on the southern flank of Broken Ridge reveal bedding structures that indicate the depth to which sedimentary rock extends within Broken Ridge (Fig. 8).

Seamounts are recognised as ecologically significant geomorphic features (Fig. 10d; Clark et al., 2011; Hein et al., 2010; Yesson et al., 2011). In the study area, four were mapped in the GSFM (Harris et al.,

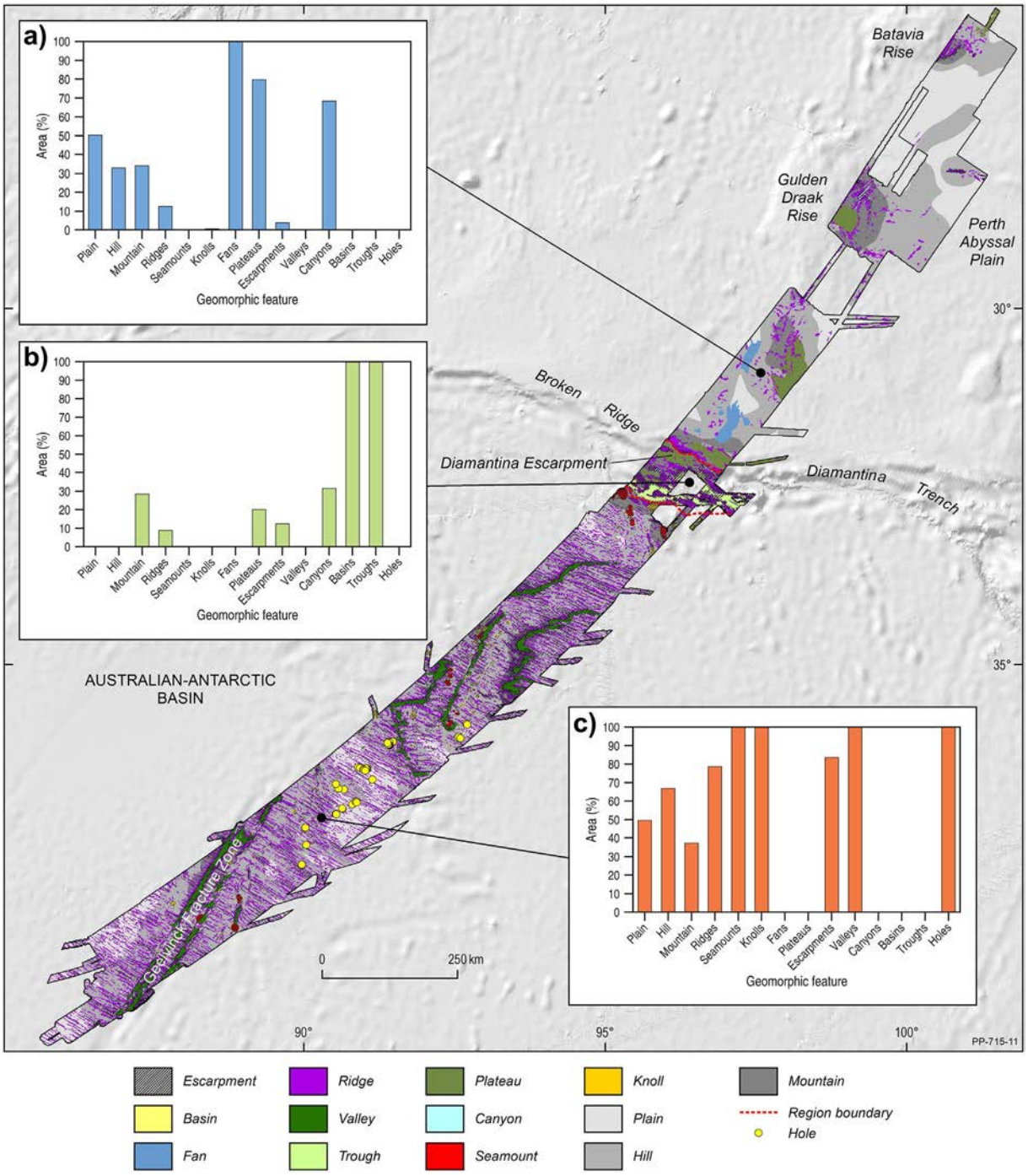

Fig. 5. MBES-derived geomorphic map with histograms showing the assemblages of features per region. a) North of Diamantina Escarpment, b) Diamantina Escarpment, and c) South of the Diamantina Trench. PP-715-11 is Geoscience Australia internal production number for this figure.

2014), whereas 17 were mapped using MBES data (Table 3). However, the 17 seamounts in the study area cover a considerably smaller total area than the four mapped in the GSFM (Table 3). These results suggest a possible similar discrepancy in the broader regional and global estimates of seamounts. For example, the Indian Ocean may contain up to four times more seamounts than estimated in the GSFM (4000 vs 1000, respectively), and the global ocean may contain several times more of these features, which are currently estimated to be between 7000 and 14,000 based on satellite altimetry and single-beam bathymetry (Agapova et al., 1979; Grid Arendal, 2015; Harris et al., 2014; Kitchingman and Lai, 2004; Wessel and Sandwell, 2010). In addition, analysis of the MBES data identified 137 sea knolls (~8 times more than seamounts), which are smaller 'seamount-like' features (250–1000 m relief). Based on the analysis of a global bathymetry grid, Kitchingman et al. (2007) identified ~100,000 sea knolls > 250 m. Sea knolls may also be significant for benthic biodiversity if, like seamounts, they interrupt bottom currents and provide hard/steep/complex benthic habitats (Grid Arendal, 2015). Clearly, as the resolution of the available global seafloor dataset improves, more sea knolls will be mapped and, given their ubiquity, more data will be required to test the significance of these features for biodiversity.

In complex areas, the minimum size of features that can be automatically picked has to be determined based on the complexity of the terrain. For example, automatic detection of sea knolls < 250 m high

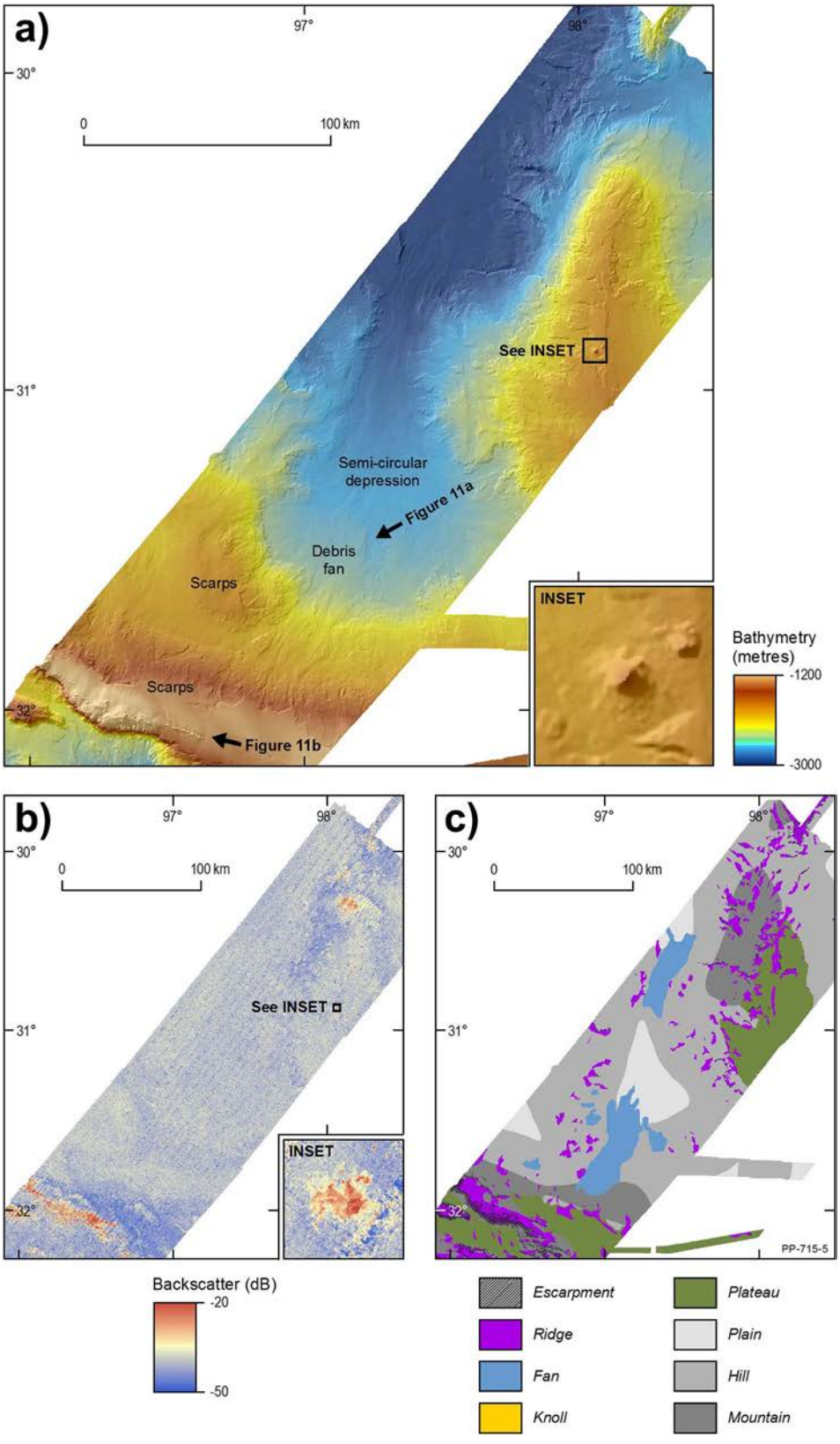

Fig. 6. Multibeam bathymetry (a), backscatter intensity (b), and geomorphic features (c) of an area north of Broken Ridge. Large arrows show the viewing direction of the 3D images presented in Fig. 11 (location shown in Fig. 1; bathymetric VE = 3). PP-715-5 is Geoscience Australia internal production number for this figure.

was not possible in this study mainly because of noise created by numerous feature types that had this level of relief (e.g., abyssal hills constituting spreading fabric). However, many 100 m high edifices interpreted as volcanic were identified visually. Thus, an automated method is less useful at fine-spatial scales, where manual interpretation is necessary to identify the full range of features. It is not always possible to relate the formation of a geomorphic feature to a specific process (or to a group of processes). For example, at the scale of the GSFM, large features can be resolved (e.g., spreading ridges, seamounts) and, to varying degrees, the tectonic processes that contributed to their

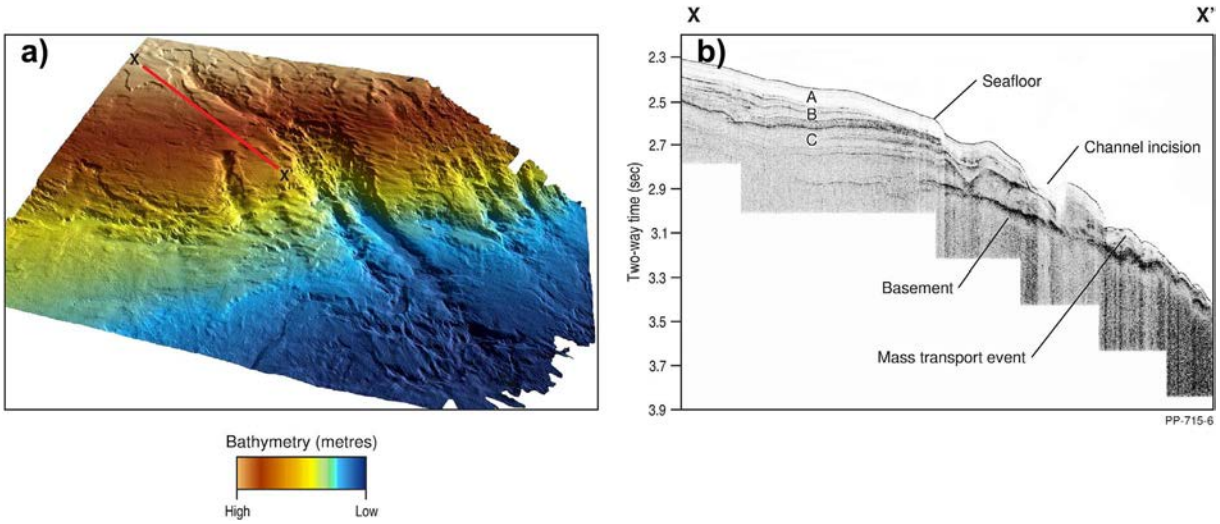

Fig. 7. a) 3D image showing canyons on the northeastern flank of Guldren Draak Rise identified in Fig. 1. b) Sub-bottom profile across the canyon region. Labels A, B, and C represent the three distinct sub-units within the marine sediment sequence (location shown in a; bathymetric VE = 5). PP-715-6 is Geoscience Australia internal production number for this figure.

formation (e.g., hotspot volcanism, plate tectonics) can be deduced. However, the ability to define smaller features (e.g., abyssal hills, pockmarks, debris flows) often allow better understanding of the seafloor processes that occur in an area.

Of the 29 types of geomorphic features described in the GSFM, ten can be directly related to their formative processes (canyon, glacial trough, spreading ridge, rift valley, fan/apron, trench, bridge, coral reef, seamount, and guyot). The other categories of the GSFM are based on rugosity (i.e., three shelf classes plus three abyssal classes) or general shape criteria (e.g., "ridges" are defined as features > 1000 m in elevation having length/width ratios > 3). Here, bathymetric and backscatter details detected for each type increase knowledge on their formative processes (e.g., valleys are fracture zones, ridges are mainly spreading fabric or detachment blocks, sea knolls are volcanoes). High-resolution bathymetry is, however, only the first step towards seafloor mapping and improving our knowledge on form-process links. Additional data, such as sub-bottom profiles, cores, and other samples, and their integration with ocean-floor maps, provide a more comprehensive ability to interpret the environmental, geological, and geophysical processes that shape the deep seabed.

5.2. Geological evolution

The history of rifting of the Kerguelen Plateau - Broken Ridge LIP and the initiation of the SEIR at > 40 Ma (Coffin et al., 2002) are recorded within the Diamantina Escarpment, which extends from the crest of Broken Ridge down to the trough known as Diamantina Trench (Fig. 8). In the MBES data, what appear to be detachment blocks (blocky ridges within plateaus) likely record rifting in which a series of grabens formed along the rift margin (Fig. 8 and 10a; as proposed in models of Chorowicz, 2005; Corti, 2009, 2012). The steep escarpment (> 1000 m high) adjoining the crest of Broken Ridge likely represents the major bounding fault on this northern margin of the rift (Fig. 10a).

The new data highlight the contrast in processes that have produced the different geological provinces north and south of the Diamantina Escarpment. Rifting, tectonism (seafloor spreading fabric, including abyssal hills and transform fault/fracture zone valleys), and seamount/sea knoll volcanism dominate the post-breakup oceanic crust of the SEIR to the south (Fig. 10), whereas marine sediment accumulation and reworking has reshaped the older oceanic crust to the north of Broken Ridge (Fig. 11). South of the Diamantina Escarpment, well-defined ridges strongly reflect the original crustal morphology rather than a younger blanket of marine sediment (Fig. 9). Conversely, the mostly flat seafloor north of Broken Ridge (Fig. 6) reflects an old igneous surface covered by > 1.5 km of marine sediment (Coffin et al., 2002; Gardner et al., 2015). In addition, most seamounts and sea knolls are located adjacent or south of the Diamantina Trench and mark volcanism synchronous with or post-dating the onset of seafloor spreading (Figs. 8 and 9). Most seamounts and sea knolls > 500 m high have multiple craters (Fig. 10d) and sit on spreading fabric formed between 10 and 40 Ma (Fig. 10b). The two sea knolls north of Broken Ridge have relatively high backscatter intensities (Fig. 6 insets), suggesting that they are not completely blanketed by marine sediment and may be relatively young.

South of Broken Ridge, a major left-stepping offset of the SEIR is preserved as the Geelvinck Fracture Zone (Figs. 1 and 9). The curvatures of the spreading fabric along the margins of the Geelvinck and other fracture zones record right-lateral transform motion. The general morphology of the fracture zones is similar to that of the Quebrada, Discovery, and Gofar transform faults systems on the East Pacific Rise (EPR; Wolfson-Schwehr et al., 2014). The major EPR transform faults (e.g., Quebrada and Gofar) are clearly defined by relatively large fault valleys, similar to the Geelvinck Fracture Zone (Fig. 9), while minor faults (e.g., Discovery Fault, Wolfson-Schwehr et al., 2014), though more complex, lack a zone of transtension, similarly to the fracture zone north of the Geelvinck (Fig. 2). Likewise, the initial stages of formation of the Discovery Fault are recorded by deep, curved depressions cutting through deformed spreading fabrics and bordered by volcanoes (− 4.25°, − 105.5°; Wolfson-Schwehr et al., 2014). This morphology resembles the two northernmost fault valleys mapped in this study (Figs. 1 and 2), suggesting that these valleys have also formed in transform faults that were active at ~25 Ma (Müller et al., 2008). The overall morphology observed here suggests a fast spreading ridge regime (Wolfson-Schwehr et al., 2014) during early seafloor spreading at the SEIR. This is consistent with the fast spreading ridge morphology close to the Amsterdam hotspot (Fig. 1), while most of the SEIR experienced an intermediate rate (Small et al., 1999).

5.3. Sediment accumulation and reworking

The new MBES data reveal extensive debris flows along the relatively flat (< 1.5°) northern flank of Broken Ridge, which correlates with previous observations from seismic reflection data (Fig. 11a; Driscoll et al., 1991). These flows mainly show a net transport of sediment from the ridge northwards into a broad, shallow depression (Fig. 6). The morphology and size of this depression is similar to the

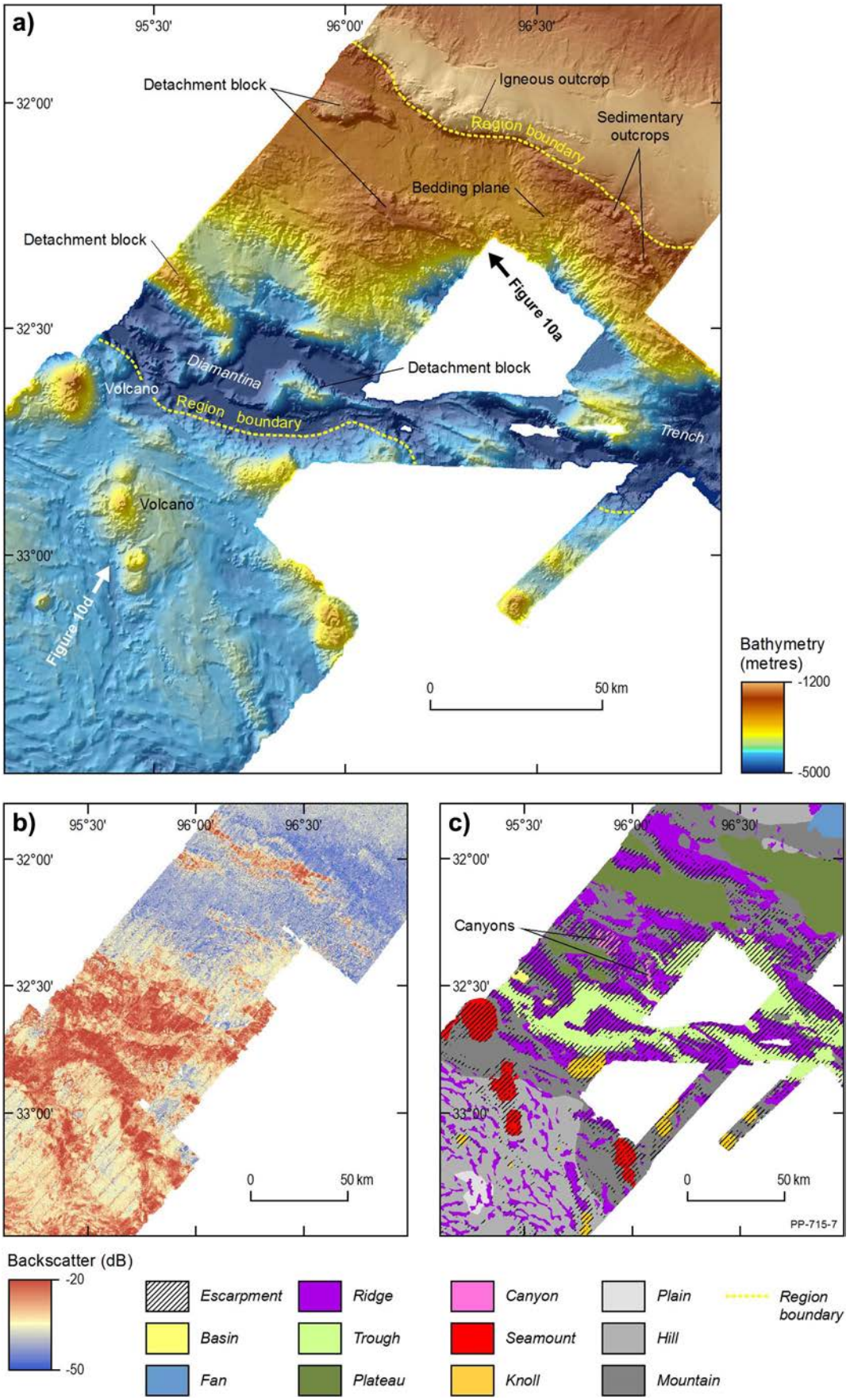

Fig. 8. Multibeam bathymetry (a), backscatter intensity (b), and geomorphic features (c) of the Diamantina Escarpment. Large arrows show the viewing direction of the 3D images presented in Fig. 10 (location shown in Fig. 1; bathymetric VE = 3). PP-715-7 is Geoscience Australia internal production number for this figure.

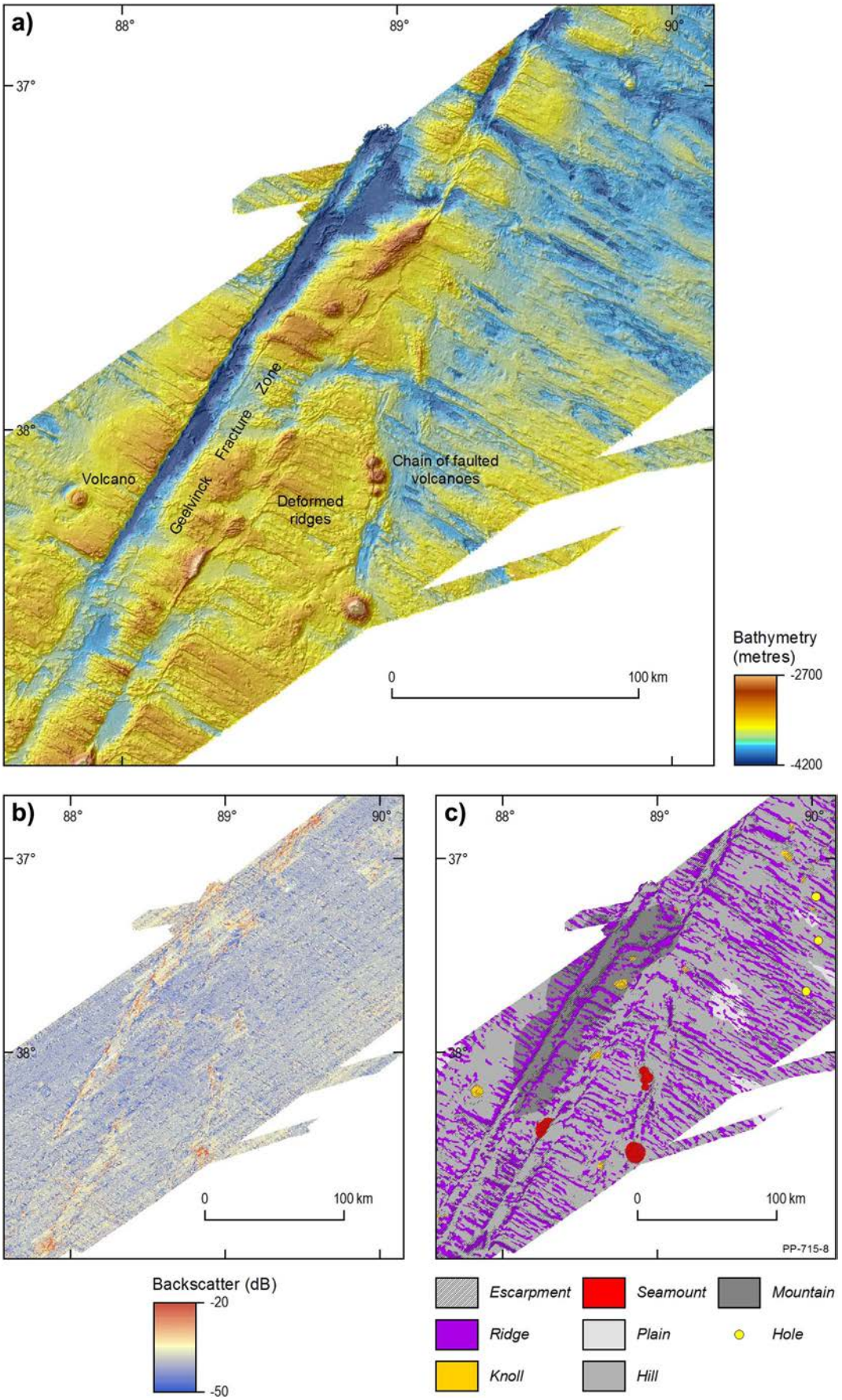

Fig. 9. Multibeam bathymetry (a), backscatter intensity (b), and geomorphic features (c) south of the Diamantina Trench, around the Geelvinck Fracture Zone. Location shown in Fig. 1. PP-715-8 is Geoscience Australia internal production number for this figure.

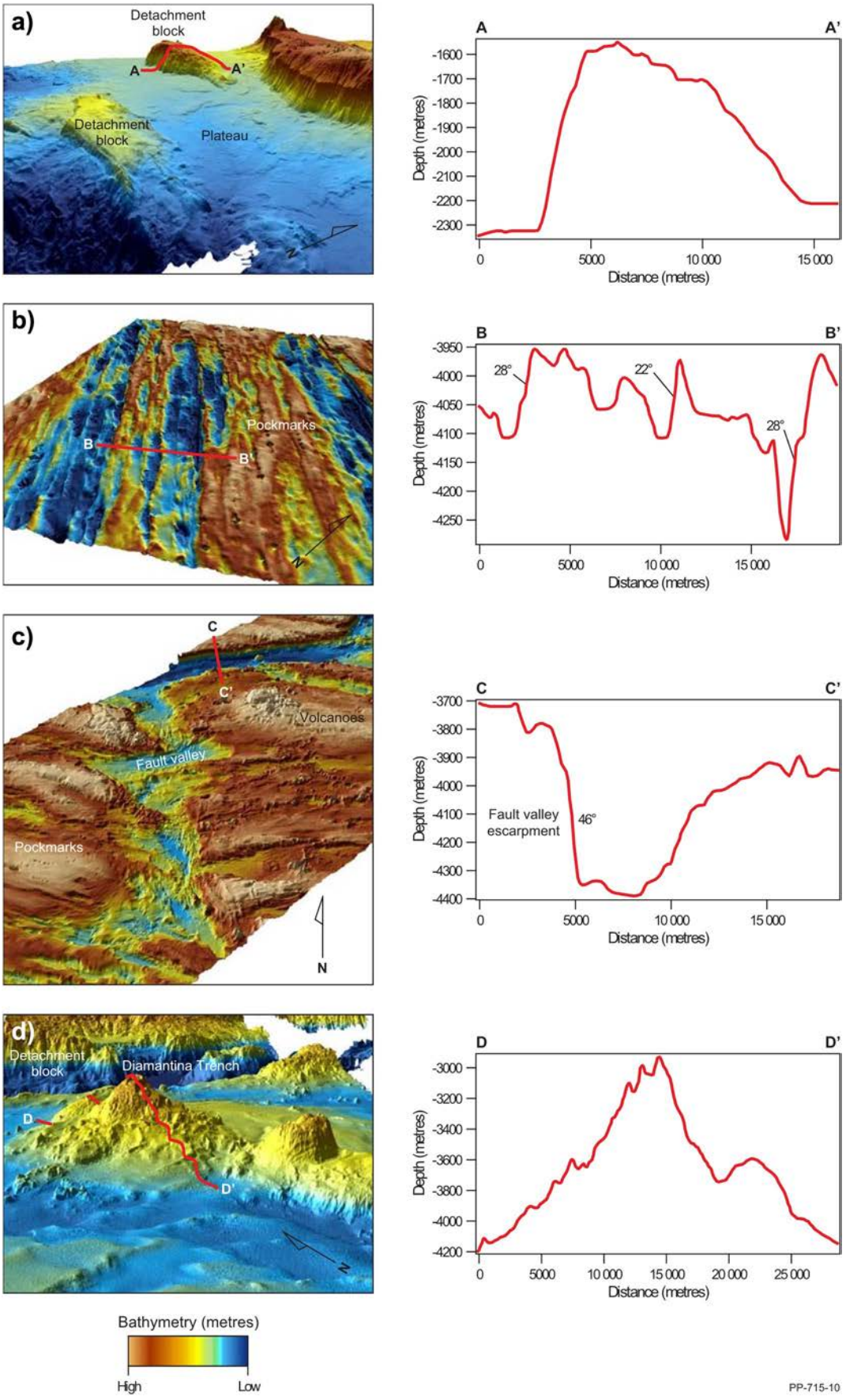

(caption on next page)

Fig. 10. Tectonic and structural processes. 3D image and cross-section of a) detachment blocks (ridges in geomorphic map) observed along a plateau immediately south of the crest of Broken Ridge (feature on the far right); b) abyssal hills/seafloor spreading fabric (ridges in geomorphic map) south of the Diamantina Escarpment; c) deformed fracture zone (valley in geomorphic map) north of the Geelvinck Fracture Zone (bathymetric VE = 5); d) volcanoes (seamounts and sea knolls in geomorphic map) immediately south of the Diamantina Trench (classified as a trough in the geomorphic map). Locations shown in Figs. 2 and 8. PP-715-10 is Geoscience Australia internal production number for this figure.

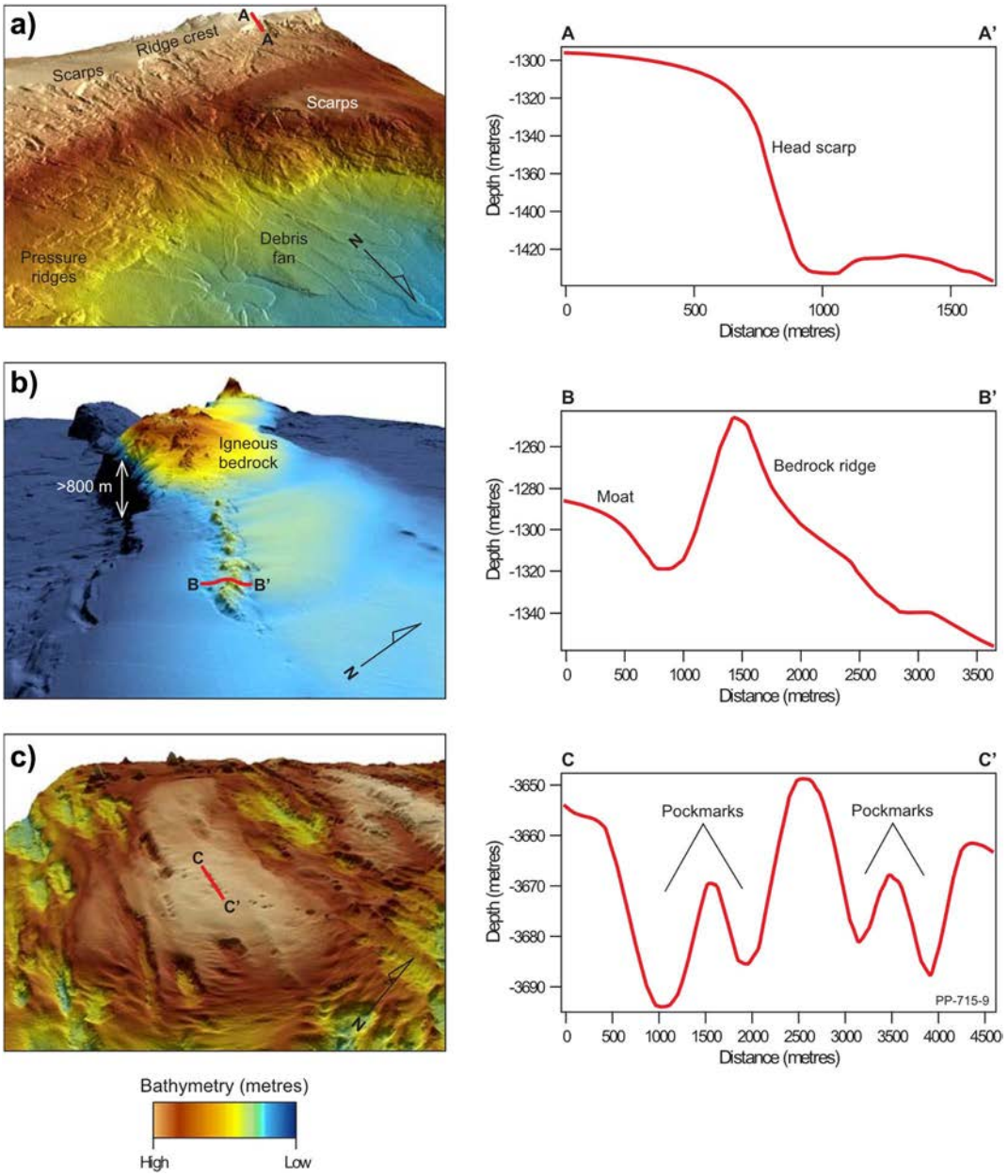

Fig. 11. Modern processes. a) 3D image of the northern flank of Broken Ridge showing many sediment mass transport features (escarpments and fans in geomorphic map) that incise the margins of the large depression identified in Fig. 6. Cross-section a-a' highlights the largest scarp (escarpment in geomorphic map). b) 3D image and cross-section of the crest of Broken Ridge showing igneous outcrops surrounded by moats produced by bottom currents (ridge in geomorphic map); and c) a chain of pockmarks (holes in geomorphic map) atop abyssal hill/seafloor spreading fabric south of the Diamantina Trench (bathymetric VE = 5). Locations show in Figs. 2 and 6. PP-715-9 is Geoscience Australia internal production number for this figure.

Bear Island scarp in the Barents Sea, suggesting that this depression may also result from a large mass transport event (Picard, 2009). A more definite interpretation of this feature will require the acquisition of additional seismic profiles. Also, although canyons are common features on passive margins, they are rare in this region and mainly confined to large escarpments attributed to rifting (Figs. 7 and 8).

Current winnowing in this region has been interpreted from observations of sediment cores acquired during previous surveys (Davies et al., 1974; Rea et al., 1990; House et al., 1991). Winnowing is also indicated by the new MBES data. For example, erosion of sediment around prominent features along the crest of Broken Ridge has formed moats (Fig. 11b). Similar features have been observed around volcanoes in comparable water depths on the Lord Howe Rise, east of Australia (Nichol et al., 2011). The smallest features detected by the new MBES data are mainly pockmarks, which we attribute to fluid or gas escape (Fig. 11c). These isolated features are only discernible south of Diamantina Trench (holes in Fig. 9c). Most are distributed linearly along ridges (abyssal hills) suggesting some basement control, most likely due to syn-sedimentary faulting in the oldest marine strata that form the hills. The hills likely focus dewatering and/or degassing of pelagic

sediment (Fig. 11c), rather than faulting in the deeper volcanic basement.

5.4. Benthic habitats

Bathymetry, backscatter and geomorphological characteristics of the seafloor vary across different benthic habitats and thus these datasets are commonly selected as useful surrogates for patterns of benthic biodiversity (Harris and Baker, 2012). This approach, which is best implemented using MBES data, is especially important in the vast deep (3000–6000 m) ocean, which forms > 75% of the ocean basins, where biodiversity is poorly mapped (Harris, 2012).

Escarpments, as well as seamounts, are common features in the MBES-based geomorphic analysis of the study area. The steepest escarpments display exposures of basement rock, providing rocky substrate for epifauna and structurally complex habitat for other organisms. Escarpments cover almost an order of magnitude greater area in the MBES-based geomorphic map than in the GSFM (Table 3 and Fig. 5; Supplement material). However, even though the number of recognised feature types increases dramatically with data resolution, the relationship between physically complex seabed and potential patterns of biodiversity in the deep ocean remains to be tested (Harris, 2012).

6. Conclusions

Our geomorphic analysis of the seafloor highlights the complexity of the area that has been searched for wreckage from flight MH370. The results demonstrate how little we know of the vast areas of ocean that have not been mapped using MBES. High resolution and accurate maps of the ocean floor are essential for providing new insights into the Earth's geological evolution, modern ocean-floor processes, and benthic habitats.

Analysis of the new MBES data shows that the ocean floor terrain is much more hilly and complex than represented in the GSFM or global bathymetric models. Compared to the GSFM, the increase in ocean floor resolution due to MBES technology allows better definition of broad-scale geomorphic features, and in most cases, increases the number of features in each feature class (e.g., 17 seamounts in MBES analyses compared to 4 in the GSFM). The power of MBES data is that it can reveal many more types of fine-scale geomorphic features (e.g., six additional feature types in the study area), which provides insights into processes acting in the region. For example, ridges occupied 2% of the study area in the GSFM, but > 20% of the seafloor in the MBES analysis. These ridges and escarpments (Broken Ridge and the Diamantina Escarpment) are significant features that record the rifting and breakup of a large igneous province. South of Broken Ridge, MBES data have revealed that spreading ridge morphology is well preserved by the numerous elongate abyssal hills that record the initiation and continued expansion of the ocean basin along the SEIR. Ecologically important features, such as seamounts and escarpments, are likewise more numerous and better resolved in the MBES data. This extensive new dataset provides an important high-resolution window into a remote region of the deep ocean, and an example of the complex ocean-floor morphology that likely exists across the remainder of the globe.

Acknowledgements

Thanks to the project team at Geoscience Australia, especially Stuart Minchin, Tanya Whiteway, Maggie Tran, and Bruce Kilgour, for the management of the project, and Silvio Mezzomo, Chris Evenden, and David Arnold for drafting the figures. The governments of Malaysia, Australia and the Peoples Republic of China agreed to undertake the underwater search for MH370 in May 2014. The Australian Transport Safety Bureau led the underwater search on behalf of the Australian Government. We thank the masters and crews of MV *Fugro Equator*, MV *Fugro Supporter*, and the Chinese naval vessel *Zhu Kezhen* for acquiring the search data. Thanks to Philip Hill, Rachel Nanson, Scott Nichol, and Larry Mayer and John Hall for their critical reviews of the manuscript. We thank Patrick De Dekker for providing legacy data information, Walter Smith for discussions around the SRTM15_plus model and Chris Carson for discussions on structural geology. We acknowledge that the search data are the result of a terrible human tragedy and we pay our respects to the 239 souls lost. This paper is published with the permission of the CEO, Geoscience Australia.

Appendix A. Supplementary data

Supplementary data to this article can be found online at https://doi.org/10.1016/j.margeo.2017.10.014.

References

Agapova, G.V., Budanova, L.Y., Zenkevich, N.L., Larina, N.I., Litvin, V.M., Marova, N.A., Rudenko, M.V., Turko, N.N., 1979. In: Neprochnov (Ed.), Geomorphology of the Ocean Floor. Geofizika okeana. Izd. Nauka, Moscow, pp. 150–205.
Argus, D.F., Gordon, R.G., DeMets, C., 2011. Geologically current motion of 56 plates relative to the no net rotation reference frame. Geochem. Geophys. Geosyst. 12 (11), 1–13.
Barnier, B., Penduff, T., Langlais, C., 2011. Eddying vs. laminar ocean circulation models and their applications. In: Schiller, A., Brassington, G.B. (Eds.), Operational Oceanography in the 21st Century. Springer, Netherlands, pp. 239–262.
Becker, J.J., Sandwell, D.T., Smith, W.H.F., Braud, J., Binder, B., Depner, J., Fabre, D., Factor, J., Ingalls, S., Kim, S.H., Ladner, R., Marks, K., Nelson, S., Pharaoh, A., Trimmer, R., Von Rosenberg, J., Wallace, G., Weatherall, P., 2009. Global bathymetry and elevation data at 30 arc seconds resolution: SRTM30_PLUS. Mar. Geod. 32, 355–371.
Berger, W.H., Winterer, E.L., 1974. Plate stratigraphy and the fluctuating carbonate line. In: Hsi, K.J., Jenkyns, H.C. (Eds.), Pelagic Sediments on Land and Under the Sea. 1. Special Publication, International Association of Sedimentologists, pp. 11–48.
Buchanan, C., Spinoccia, M., Picard, K., Wilson, O., Sexton, M.J., Hodgkin, S., Parums, R., Siwabessy, P.J.W., 2013. Standard Operation Procedure for a Multibeam Survey: Acquisition & Processing. Geoscience Australia, Canberra.
Chorowicz, J., 2005. The East African rift system. J. Afr. Earth Sci. 43, 379–410.
Clark, M.R., Watling, L., Rowden, A.A., Guinotte, J.M., Smith, C.R., 2011. A global seamount classification to aid the scientific design of marine protected area networks. Ocean Coast. Manag. 54, 19–36.
Coffin, M.F., Eldholm, O., 1994. Large igneous provinces: crustal structure, dimensions, and external consequences. Rev. Geophys. 32, 1–36.
Coffin, M.F., Frey, F.A., Wallace, P.J., et al., 2000. Proceedings of the Ocean Drilling Program, Initial Reports.
Coffin, M.F., Pringle, M.S., Duncan, R.A., Gladczenko, T.P., Storey, M., Müller, R.D., Gahagan, L.A., 2002. Kerguelen hotspot magma output since 130 Ma. J. Petrol. 43, 1121–1137.
Corti, G., 2009. Continental rift evolution: from rift initiation to incipient break-up in the main Ethiopian rift, East Africa. Earth Sci. Rev. 96, 1–53.
Corti, G., 2012. Evolution and characteristics of continental rifting: analog modeling-inspired view and comparison with examples from the East African rift system. Tectonophysics 522–523, 1–33.
Davies, T.A., Luyendyk, B.P., Rodolfo, K.S., Kempe, D.R.C., McKelvey, B.C., Leidy, R.D., Horvath, G.J., Hyndman, R.D., Thierstein, H.R., Herb, R.C., Boltovskoy, E., Doyle, P., 1974. Site 255. In: Luyendyk, B.P., Davies, T.A. (Eds.), Results of DSDP Leg 26 and the geological history of the southern Indian Ocean. Ocean Drilling Program, College Station, TX, United States, pp. 281–294.
DeMets, C., Gordon, R.G., Argus, D.F., 2010. Geologically current plate motions. Geophys. J. Int. 181, 1–80.
Driscoll, N.W., Karner, G.D., Weissel, J., Party, S.S., 1991. Stratigraphic and tectonic evolution of Broken Ridge from seismic stratigraphy and Leg 121 drilling. In: Weissel, J., Pierce, J., Taylor, E., Alt, J. (Eds.), Proceedings of Ocean Drilling Program, Scientific Results. ODP, College Station, Texas, pp. 71–91.
Duncan, R.A., 2002. A time frame for construction of the Kerguelen plateau and broken ridge. J. Petrol. 43, 1109–1119.
Fonseca, L., Calder, B., 2005. In: Geocoder: An Efficient Backscatter Map Constructor. Proceedings of the U.S. Hydrographic Conference 2005, San Diego.
Gaina, C., Müller, R.D., Brown, B., Ishihara, T., Ivanov, S., 2007. Breakup and early seafloor spreading between India and Antarctica. Geophys. J. Int. 170, 151–169.
Gardner, R.L., Daczko, N.R., Halpin, J.A., Whittaker, J.M., 2015. Discovery of a micro-continent (Gulden Draak Knoll) offshore Western Australia: implications for East Gondwana reconstructions. Gondwana Res. 28, 1019–1031.
Grid Arendal, 2015. Blue Habitats. Grid Arendal. Retrieved from. https://www.bluehabitats.org/?page_id=1678.
Hamblin, W.K., Christiansen, E.H., 2004. Earth's Dynamic Systems, 10 ed. Prentice Hall Inc., Upper Saddle River.
Harris, P.T., 2012. Surrogacy. In: Harris, P.T., Baker, E.T. (Eds.), Seafloor Geomorphology as Benthic Habitat. Elsevier, London, pp. 93–108.
Harris, P.T., Baker, E.K., 2012. Why map benthic habitats? In: Harris, P.T., Baker, E.T. (Eds.), Seafloor Geomorphology as Benthic Habitat. Elsevier, London, pp. 3–22.
Harris, P.T., Macmillan-Lawler, M., Rupp, J., Baker, E.K., 2014. Geomorphology of the

oceans. Mar. Geol. 352, 4–24.
Hayes, D.E., Kane, K.A., 1994. Long-lived mid-ocean ridge segmentation of the Pacific-Antarctic ridge and the Southeast Indian ridge. J. Geophys. Res. Solid Earth 99, 19679–19692.
Hein, J.R., Conrad, T.A., Staudigel, H., 2010. Seamount mineral deposits: a source of rare metals for high-technology industries. Oceanography 23, 184–189.
Hollister, C.D., 1993. The concept of deep sea contourites. Sediment. Geol. 82, 5–15.
House, M.A., Rea, D.K., Janecek, T.R., 1991. Grain-size record of ocean current winnowing in oligocene to pleistocene ooze, Broken Ridge, Southeastern Indian Ocean. In: Weissel, J., Pierce, J., Taylor, E., Alt, J. (Eds.), Proceedings of Ocean Drilling Program, Scientific Results. ODP, College Station, Texas, pp. 211–218.
IHO, 2013. Standardization of Undersea Feature Names: Guidelines Proposal Form Terminology, 4.1.0 ed. International Hydrographic Organisation and Intergovernmental Oceanographic Commission, Monaco, pp. 32.
Karner, G.D., Driscoll, N.W., 1993. Rift flank topography and extensional basin architecture: formation of broken ridge, southeast Indian Ocean. An. Acad. Bras. Cienc. 65, 293–294.
Kennett, J.P., Watkins, N.D., 1975. Deep sea erosion and manganese nodule pavement development in the South and Indian Ocean. Science 188, 1011–1013.
Kidd, R.B., Davies, T.A., 1978. Indian Ocean sediment distribution since Late Jurassic. In: Borch, V.D. (Ed.), Synthesis of Deep-Sea Drilling Results in the Indian Ocean. Elsevier, Amsterdam.
Kitchingman, A., Lai, S., 2004. Inferences on potential seamount locations from mid-resolution bathymetric data. In: Morato, T., Pauly, D. (Eds.), FCRR Seamounts: Biodiversity and Fisheries. Fisheries Centre Research Reports. University of British Columbia, Vancouver, pp. 7–12.
Kitchingman, A., Lai, S., Morato, T., Pauly, D., 2007. How many seamounts are there and where are they located. In: Pitcher, T.J., Morato, T., Hart, P.J.B., Clark, M.R., Haggan, N., Santos, R.S. (Eds.), Seamounts: Ecology, Fisheries, and Conservation. Blackwell Publishing, Oxford, pp. 26–40.
Lamarche, G., Lurton, X., 2017. Recommendations for improved and coherent acquisition and processing of backscatter data from seafloor-mapping sonars. Mar. Geophys. Res. 1–18.
Müller, R.D., Royer, J.-Y., lawver, L.A., 1993. Revised plate motions relative to the hotspots from combined Atlantic and Indian Ocean hotspot tracks. Geology 21, 275–278.
Müller, R.D., Sdrolias, M., Gaina, C., Roest, W.R., 2008. Age, spreading rates, and spreading asymmetry of the world's ocean crust. Geochem. Geophys. Geosyst. 9, 1–19.
Neal, C.R., Mahoney, J.J., Chazey, W.J., 2002. Mantle sources and the highly variable role of continental lithosphere in basalt petrogenesis of the Kerguelen Plateau and Broken Ridge LIP: results from ODP leg 183. J. Petrol. 43, 1177–1205.
Nichol, S.L., Heap, A.D., Daniell, J., 2011. High resolution geomorphic map of a submerged marginal plateau, northern Lord Howe Rise, east Australian margin. Deep-Sea Res. II Top. Stud. Oceanogr. 58 (7–8), 889–898.
Olson, C.J., Becker, J.J., Sandwell, D.T., 2016. SRTM15_PLUS: Data Fusion of Shuttle Radar Topography Mission (SRTM) Land Topography With Measured and Estimated Seafloor Topography (NCEI Accession 0150537). Version 1.1. NOAA National Centers for Environmental Information Dataset. [January, 2017].
Picard, K., 2009. The Bornoya Slide Scar Revealed Through High-resolution Bathymetric Date, SW Barents Sea Shelf Margin, International Conference on Seafloor Mapping for Geohazard Assessment. Società Geologica Italiana, Italy, pp. 187–189.
Picard, K., Brooke, B.P., Coffin, M.F., 2017a. Geological Insights From Malaysia Airlines Flight MH370 Search, Eos.
Picard, K., Smith, W.H., Tran, M., Siwabessy, J.P., Kennedy, P., 2017b. Increased Resolution Bathymetry in the Southeast Indian Ocean, Hydro International Magazine, 28 September 2017.
Pierce, J., Weissel, J., et al., 1989. Proceedings ODP. Initial Reports 5–31.
Rea, D.K., Dehn, J., Driscoll, N.W., Farrell, J.W., Janecek, T.R., Owen, R.M., Pospichal, J.J., Resiwati, P., 1990. Paleoceanography of the Eastern Indian-Ocean from ODP Leg-121 drilling on broken ridge. Geol. Soc. Am. Bull. 102, 679–690.
Russo, C.J., Rubin, K.H., Graham, D.W., 2009. Mantle melting and magma supply to the Southeast Indian ridge: the roles of lithology and melting conditions from U-series disequilibria. Earth Planet. Sci. Lett. 278, 55–66.
Siwabessy, P.J.W., Tran, M., Picard, K., et al., 2017. Mar. Geophys. Res. http://dx.doi.org/10.1007/s11001-017-9314-7. (21 p.).
Small, C., Cochran, J.R., Sempéré, J.-C., Christie, D., 1999. The structure and segmentation of the Southeast Indian Ridge. Mar. Geol. 161, 1–12.
Smith, W.H.F., 1993. On the accuracy of digital bathymetric data. J. Geophys. Res. 98, 9591–9603.
Smith, W.H.F., Sandwell, D.T., 1997. Global sea floor topography from satellite altimetry and ship depth soundings. Science 277, 1956–1962.
Smith, W.H.F., Marks, K.M., Schmitt, T., 2017. Airline Flight Paths Over the Unmapped Ocean, Eos. pp. 98. http://dx.doi.org/10.1029/2017EO069127. Published on 08 March 2017.
Wallace, D.J., Frey, F.A., Weis, D., Coffin, M.F., 2002. Origin and evolution of the Kerguelen plateau, Broken Ridge and Kerguelen archipelago. J. Petrol. 43, 1105–1108.
Weatherall, P., Marks, K.M., Jakobsson, M., Schmitt, T., Tani, S., Arndt, J.E., Rovere, M., Chayes, D., Ferrini, V., Wigley, R., 2015. A new digital bathymetric model of the world's oceans. Earth and Space Science 2, 331–345.
Wessel, P., Sandwell, D.T., 2010. The global seamount census. Oceanography 23, 24–33.
Whittaker, J.M., Goncharov, A., Williams, S.E., Müller, R.D., Leitchenkov, G., 2013. Global sediment thickness data set updated for the Australian-Antarctic Southern Ocean. Geochem. Geophys. Geosyst. 14, 3297–3305.
Wolfson-Schwehr, M., Boettcher, M.S., McGuire, J.J., Collins, J.A., 2014. The relationship between seismicity and fault structure on the discovery transform fault, East Pacific rise. Geochem. Geophys. Geosyst. 15, 3698–3712.
Yesson, C., Clark, M.R., Taylor, M.L., Rogers, A.D., 2011. The global distribution of seamounts based on 30 arc seconds bathymetry data. Deep-Sea Res. I Oceanogr. Res. Pap. 58, 442–453.